Precise calcium-to-spike inference using biophysical generative models

Gerard Joey Broussard[1], Giovanni Diana[2], Francisco J. Urra Quiroz[2], Berat Semichan Sermet[2], Laura A. Lynch[1], David A. DiGregorio[2,3,] *, Samuel S.-H. Wang[1,] *

[1]Neuroscience Institute, Washington Road, Princeton University, Princeton, New Jersey USA 08540.

[2]Institut Pasteur, Université Paris Cité, CNRS UMR 3571, Synapse and Circuit Dynamics Laboratory, Paris, France.

[3]Department of Physiology and Biophysics, University of Colorado School of Medicine, Aurora, Colorado

*co-Senior authors

Correspondence: sswang@princeton.edu; david.digregorio@cuasnchutz.edu

Acknowledgements: The authors thank Marissa Applegate, Kiri Couchman, and Minglu Wang for collaboration and technical assistance in early stages of this project. S.W. was supported by NIH R01 NS045193 and U19 NS104648. S.W. and D.D. were supported by NIH R21 EY026434. G.J.B. was supported by the Warren Alpert Foundation and the Brain & Behavior Research Foundation. The laboratory of D.D. was also supported by the Fondation pour la Recherche Médicale (FRM EQU202003010555), Fondation pour l'Audition (FPA-RD-2018-8), and the Agence Nationale de la Recherche (ANR-17-CE16-0019, and ANR-18-CE16-0018, ANR-19-CE16 0019-02, ANR-21-CE16-0036-01).

Abstract

The nonlinear intramolecular dynamics of fluorescent indicators of neural activity can distort the accurate estimate of action potential (“spike”) times. In order to develop a more accurate spike inference algorithm we characterized the kinetic responses to different calcium concentrations of three popular calcium indicators (GCaMP6f, jGCaMP7f, and jGCaMP8f) using in vitro stopped-flow and brain slice recordings. jGCaMP8f showed a use-dependent slowing of fluorescence responses that caused existing inference methods to generate numerous false positives. From these data we developed multistate models of GcaMPs and used them to create a Bayesian Sequential Monte Carlo ($\text{Biophys}_{\text{SMC}}$) and machine learning ($\text{Biophys}_{\text{ML}}$) inference methods that largely reduced false positives and improved the spike time accuracy from publicly available ground-truth data. The $\text{Biophys}_{\text{SMC}}$ method detected individual spikes with an average uncertainty of 6 milliseconds, a 6-fold improvement over previous methods. Our framework highlights the advantages of physical model-based approaches over model-free algorithms.

Introduction

Genetically encoded calcium indicators (GECIs), as exemplified by the GCaMP family of sensors (Tian et al., 2009; Akerboom et al., 2012; Chen et al., 2013; Dana et al., 2019; Zhang et al., 2023), have transformed the study of neural populations by enabling simultaneous recordings from large ensembles of neurons (Demas et al., 2021). These sensors convert rapid changes in intracellular calcium concentration, which accompany neuronal action potentials, into measurable fluorescence signals. However, the temporal resolution of GECIs is limited by their slower kinetics compared to the rapid voltage changes associated with neuronal spikes. This mismatch limits the temporal precision with which the neural dynamics underlying behavior can be accurately estimated (Xiao et al., 2017; Li et al., 2019; Wei et al., 2020).

A variety of computational strategies have been developed to address the challenge of inferring spikes from fluorescence signals. These methods can be broadly categorized as either supervised or unsupervised. Supervised approaches leverage training data where both fluorescence and spike times are known to train machine learning models to recognize statistical regularities mapping observed signals to underlying spiking activity (Rupprecht et al., 2021; Zhou et al., 2023). Unsupervised approaches, by contrast, do not require labeled data and instead use principled assumptions about how spikes generate fluorescence based on the statistical properties of fluorescence time series to infer latent spike trains (e.g. Vogelstein et al., 2010; Pnevmatikakis et al., 2013; Deneux et al., 2016; Friedrich et al., 2017; Sebastian et al., 2017; Pachitariu et al., 2018). The performance of both categories is enhanced under the assumption that the relationship between spike occurrences and the resultant fluorescence responses is fundamentally linear. When this linearity assumption holds, unsupervised methods can utilize simple, computationally efficient models (in particular linear deconvolution; Friedrich et al., 2017), while supervised methods benefit from stable, direct mappings that allow for robust training and generalization.

However, the spike-to-fluorescence relationship often deviates from the linear ideal. Classic examples include saturation of indicator fluorescence at high calcium concentrations (Regehr and Atluri, 1995) and slowing of calcium dynamics due to calcium buffering by high-affinity indicators (Sabatini and Regehr, 1998). Thirdly, GECI responses to free calcium changes can be supralinear (Rose et al., 2014). Such nonlinearities pose potential challenges to both unsupervised and supervised methods. Popular unsupervised methods relying on low-complexity models such as linear convolution or generative frameworks reliant upon a static decay process would be expected to exhibit systematic errors dictated by the nature of the nonlinearity. Supervised methods, meanwhile, may fail to capture the complexity of novel, nonlinear regimes that differ substantially from the conditions under which they were trained (Seroussi and Zeitouni, 2022; Sariyildiz et al., 2023). Consequently, nonlinearities in the spike-to-fluorescence transformation have the potential to degrade the accuracy and reliability of inferred spike statistics.

The recently developed jGCaMP8 sensors represent a promising advance due to their faster rise times and improved single-spike signal-to-noise ratios (SNR) (Zhang et al., 2023; Diana et al., 2024), but little is known about what new non-linearities are introduced by them. In several reports, past generation indicators have been reported to exhibit supralinear responses arising from closely occurring spikes (Chen et al., 2013; Éltes et al., 2019; Wei et al., 2020;

Huang et al., 2021; Schoenfeld et al., 2021). Neither models designed to capture this supralinearity (Deneux et al., 2016; Wei et al., 2020) nor models that assume linear characteristics of the newer probes (Zhang et al., 2023) are able to extract more accurate spiking dynamics using jGCaMP8 than from previous-generation sensors.

To address these gaps, we first comprehensively characterized the dynamics of GCaMP6f, jGCaMP7f, and jGCaMP8f responses. We identified novel nonlinear properties of these responses, including a pronounced use-dependent slowing by jGCaMPf during periods of heightened activity. We developed a biophysical model of all three GCaMPs and used it as the core of two new spike inference approaches: a sequential Monte Carlo (SMC) method to model latent spike-time sequences, and a machine learning-based strategy trained on synthetic data generated by the SMC model. Both approaches identify spike times with higher accuracy and temporal precision than any currently used technique.

Results

jGCaMP8 variants have been reported to possess improved kinetic properties and linear responses to action potentials compared to earlier GCaMP versions (Zhang et al., 2023). To precisely quantify these improvements, we expressed GCaMP6f, jGCaMP7f, or jGCaMP8f in cerebellar granule cells using adeno-associated viral vectors. High-speed (0.5-1 kHz) two-photon line scan imaging was used to measure fluorescence transients in single boutons (parallel fibers, PFs; **Figure 1A-C**) in response to extracellularly-evoked action potentials. jGCaMP8f exhibited the fastest rise and decay times (**Figure 1C**), largest fractional fluorescence changes (**Figure 1D**) (GCaMP6f, 0.29±0.04, n = 14 boutons; jGCaMP7f, 0.34±0.05, n = 27; jGCaMP8f, 0.59±0.07, n = 32; the small-molecular indicator Oregon Green BAPTA-5N, OGB-5N, 0.39±0.04, n = 11; mean± SEM; ANOVA, p = 0.0041; significant Tukey HSD post hoc comparisons: p = 0.01 GCaMP6f vs. jGCaMP8f and jGCaMP7f vs. jGCaMP8f), and highest signal-to-noise ratios (**Figure 1E**) (GCaMP6f, 1.41±0.19; jGCaMP7f, 1.3±0.2; jGCaMP8f, 5.6±0.1; mean± SEM; ANOVA, p = 6.7e-10; significant Tukey HSD post hoc comparisons: p = 1.6e-6, GCaMP6f vs. jGCaMP8f; p = 5.2e-9, (jGCaMP7f, jGCaMP8f) compared to other GCaMPs. The rise time of jGCaMP8f approached that of OGB-5N, which is known for its near diffusion-limited calcium on-binding kinetics (DiGregorio et al., 1999) (**Figure 1F**; GCaMP6f, 18.1±1.6 ms; jGCaMP7f, 13.7±0.7 ms; jGCaMP8f, 3.1±0.2 ms; OGB-5N, 0.3±0.1 ms; mean± SEM; ANOVA test, p = 6.7e-29; significant Tukey HSD post hoc comparisons: p = 1.1e-21, GCaMP6f vs. OGB5N; p = 5.4e-4, jGCaMP6f vs. jGCaMP7f; p = 3.9e-23, jGCaMP6f vs. jGCaMP8f; p = 8.7e-18, jGCaMP7f vs. OGB-5N; p = 1.5e-19, jGCaMP7f vs. jGCaMP8f).

Recent reports of GCaMP6 indicators suggest a nonlinear relationship between the number of APs and the corresponding fluorescence response (Wei et al., 2020; Huang et al., 2021; Zhang et al., 2023). To quantify the time-dependence of this nonlinearity across fast indicator variants, we explored signals evoked by pairs of spikes delivered at defined time intervals. GCaMP6f and GCaMP7f showed short-term supralinearity that decreased to a linear summation for spike intervals greater than 100 ms (**Figure 1G, H**) (GCaMP6f, 3.1±0.7 at 10 ms and 1.5±0.3 at 100 ms fold increase, n = 7 boutons; jGCaMP7f, 1.9±0.2 at 10 ms and 1.1±0.1 at 100 ms, n = 14 boutons; mean± SEM; two-way mixed ANOVA, $F(3,60) = 7.2$, p = 3.3e-4 main effect of indicator, with significant one-way ANOVA at 10 ms, $F(3,32) = 6.4$, p = 0.0016;

significant Tukey HSD post hoc comparisons: p = 0.01, GCaMP6f vs. OGB-5N). In contrast, the jGCaMP8f responses were near linear in their response amplitude to spikes at all tested intervals (**Figure 1G, H**) (testing against a null distribution centered on 1; one-sample t-test, p = 0.32).

To examine responses to bursts of activity, we measured bouton fluorescence in response to 1, 2, and 10 AP stimuli delivered at 100 Hz. GCaMP6f responses showed a strong supralinearity, in which a 10-pulse train evoked signals approximately 20-fold larger than a single pulse (**Figure 1G**, top), consistent with positive cooperativity. In contrast, jGCaMP8f responses under the same comparison resulted in only a 3-fold larger response (**Figure 1F**, bottom). These findings were broadly consistent indicator saturation and low apparent cooperativity (**Figure 1F**, bottom).

Unexpectedly, all three tested GCaMPs showed a slowing of the decay of fluorescence transients driven by ten spikes compared with a single spike (**Figure 1I**) (GCaMP6f, 78±5 ms 1 pulse vs. 130±9 ms 10 pulse, n = 6 boutons; jGCaMP7f, 77±5 ms 1 pulse vs. 126±7 ms 10 pulse, n = 22 boutons; jGCaMP8f, 41±3 ms 1 pulse vs. 123±12 ms 10 pulse, n = 14 boutons; mean± SEM; two-way mixed ANOVA, $F(1,78) = 72.2$, p = 1.0e-12 main effect of time). This use-dependent effect was particularly pronounced for jGCaMP8f (~3-fold slowing) when compared to the older fast sensor variants (~1.5-fold slowing) (**Figure 1J, K**). Further analysis revealed that a two-component exponential was required to achieve acceptable fits to the decay even for most single spike responses. Both kinetic components tended to increase in duration with the number of spikes (**Supplementary Figure 1**).

To explore the impact of nonlinear properties of the old and new GCaMP variants, we compared experimentally-measured spike responses to a linear model. This was achieved by convolving a kernel fitted to a single spike response with the spike train used to generate the observed data. In the paired-spike protocol, the GCaMP6f kernel underestimated the response to a 10 ms inter-spike interval, a condition under which the amplitude nonlinearity is largest. The estimate improves as the intervals lengthen and the nonlinearity decreases (**Figure 1J**). When jGCaMP8f boutons were exposed to a 10 Hz Poisson stimulus train, the kernel estimate diverged increasingly from the real data (**Figure 1K**). Overall, these analyses reveal that the GCaMP6f amplitude nonlinearity is dependent on spike timing, while the use-dependent slowing of jGCaMP8f signals is dependent on spike rate. These findings indicate activity regimes where linear methods for deconvolution are expected to be unsuccessful: short inter-spike intervals for older GCaMPs, and high spike rates for jGCaMP8f.

To gain insight into the mechanistic basis for GCaMP's use-dependent nonlinearities, we measured GCaMP fluorescence responses to various calcium concentration steps directly using stopped-flow fluorimetry on purified protein (**Figure 2A, B)**. We first optimized stopped-flow buffer conditions to closely match intracellular ionic composition, including magnesium, which we found to be necessary to reproduce the kinetics and dynamic range of the GCaMP responses observed in living cells (**Supplementary Figure 2, 3**). The rise and decay kinetics of jGCaMP8f were faster than 6f and 7f for all calcium concentration steps in the range of 0-10 μM (**Figure 2C, D**). Within the range of calcium increase expected in response to a small number of spikes (shaded region, **Figure 2E**), the rise time of spike-evoked calcium transients for each GECI variant correlated with stopped-flow rise times (**Figure 2E, F**). Similarly, the paired-pulse facilitation of a GCaMP's fluorescent response in neurons closely tracked cooperativity

measures derived from analysis of the early stopped-flow response (**Figure 2G-I**). These experiments show that our stopped-flow measurements capture key features of action potential-evoked calcium responses in neurons.

Previous studies showed that activation of GCaMPs by calcium can occur via a fast and a slow pathway (Sun et al., 2013; Badura et al., 2014).Closer inspection of the binding and unbinding kinetics across GCaMP sensors revealed fast and slow phases of fluorescence increases. Responses of GCaMP6f and jGCaMP7f arose predominantly from a slow component whose speed increased with the size of the calcium step. In contrast, jGCaMP8f's fluorescence developed predominantly through a fast component. While both kinetic components contributed to fluorescence changes in all GECIs, jGCaMP8f was distinguished by having a faster and larger contribution from the fast component at all concentrations tested (**Figure 2J**, **Supplementary Figure 4**).

The presence of two time constants in the rising phase of the fluorescence response is consistent with entrance into at least two distinct fluorescence states. The presence of multiple fluorescence states could account for fast and slow decay rates. We compared the time constants governing this fast and slow increase to the use-dependent slowing effect observed in our ex vivo (i.e. brain slice) recordings . We found a linear relationship between our ex vivo observations and a metric we term accessible slowing which represents a tradeoff between the speed of entrance into the fast versus slow state and stability of the slow state (**Figure 2K, L**). These observations support the conclusion that large calcium increases push GCaMPs into a stable fluorescent state from which they are slow to exit.

Multiple kinetic pathways are known to coexist in the calcium-sensing domain of GCaMP, calmodulin, which semi-independently binds calcium via its N-lobe (fast-binding) and C-lobe (slow-binding) (Linse et al., 1991; Faas et al., 2011), each subsequently capable of interacting with a target peptide to induce fluorescence (Johnson et al., 1996; Brown et al., 1997; Sun et al., 2013; Lai et al., 2015). . We therefore incorporated parallel fast and slow kinetic pathways to multiple fluorescence states into a biophysical model of GCaMP to account for our *in vitro* and *ex vivo* observations (**Figure 3A**).

In order to fit the GCaMP model to experimental data, we took advantage of a neuron type (cerebellar granule cells) with well-characterized calcium buffering and handling (Rebola et al., 2019). The cell model used here included endogenous buffering, calcium extrusion mechanisms, and calcium exchange from intracellular stores (**Figure 3B**) and could reproduce the fast dynamics of previous buffer models (Rebola et al., 2019), but we also added a second compartment to account for a slow decay that was not used to constrain previous models. By jointly fitting the stopped-flow data and *ex vivo* responses, we derived the final GCaMP model parameters for each variant, which were then fixed for all subsequent analyses (**Supplementary Figure 5; Supplementary Figure 6A, B**). This approach allowed us to faithfully reproduce observations from all experimental systems and GCaMP variants, despite the idiosyncrasies observed across the sensors (**Figure 3C, D; Supplementary Figure 6C-F**).

Further analyses of the GCaMP model states (**Figure 3A; Supplementary Figure 6A**) revealed additional insights into how parameterization led to different operational modes. When separating the fluorescent GCaMP model states into those that depended on C-lobe binding (slow fluorescent) and those that did not (fast fluorescent), we observed that jGCaMP8f alone showed stable occupancy of the fast fluorescent states in both stopped-flow and ex vivo fits

(**Figure 3E; Supplementary Figure 6C-F**). The slowing of jGCaMP8f responses following spike bursts, in contrast, was driven by increased occupancy of a slow, fluorescent and non-fluorescent state (**Figure 3E**, blue and gray, respectively).

We next leveraged the GCaMP model to implement a generative spike inference algorithm. Inspired by recent successes of a Bayesian autoregressive-model based approach (Diana et al. 2024), we adopted the same Sequential Monte Carlo (SMC) framework in which time-invariant parameters (such as those governing cell calcium handling) and latent states (such as spike times) are jointly estimated in an iterative manner to estimate spike times (**Supplementary Figure 7**).

As an initial test of this approach, we generated ground truth simulations using the GCaMP model and attempted inference using our SMC framework with either the GCaMP model ($\text{Biophys}_{\text{SMC}}$ hereafter) or a linear autoregressive model ($\text{Linear}_{\text{SMC}}$) as the generative model (**Figure 3F, G**).Using this approach, $\text{Linear}_{\text{SMC}}$ produced a progressive increase in the number of false spike predictions during periods of elevated spiking for both cell types, particularly in the decay phase of the fluorescence. This is likely due to the use-dependent slowing in the decay. In contrast, $\text{Biophys}_{\text{SMC}}$, which accommodated all nonlinearities, made consistent, accurate predictions of spike times across the simulation epoch. The $\text{Biophys}_{\text{SMC}}$ was able to reproduce the input spike train with higher accuracy and precision in the context of simulations designed to mimic different cell types, including both excitatory and inhibitory cells.

The $\text{Biophys}_{\text{SMC}}$ approach to spike inference is computationally time-consuming due to the SMC sampling. Therefore we used the GCaMP model to create a synthetic training dataset for a machine learning algorithm (Rupprecht 2021). Specifically, we generated synthetic fluorescence data for training using cell parameters derived from the $\text{Biophys}_{\text{SMC}}$ along with randomly generated spikes, noise, and baseline drift designed to mimic the statistics of the dataset targeted for inference (**Figure 4A**). In this way, we obtained two methods for spike inference: an unsupervised Bayesian approach ($\text{Biophys}_{\text{SMC}}$), and a faster supervised machine-learning approach ($\text{Biophys}_{\text{ML}}$).

We benchmarked our spike inference methods against current state-of-the-art supervised and unsupervised approaches for spike inference on excitatory and inhibitory cell responses from the jGCaMP8f dataset (Zhang et al., 2023). We used 142 8.2-second epochs of firing in 37 excitatory neurons, containing 5,817 ground truth action potentials, with 31±24 spikes per epoch (median±estimated SD). For the generative methods, we compared our Bayesian approach ($\text{Biophys}_{\text{SMC}}$) against MLspike, an established algorithm based on an alternative generative model of calcium-fluorescence dynamics (Deneux et al., 2016). For the supervised methods, we compared our trained networks ($\text{Biophys}_{\text{ML}}$) against the CASCADE (Rupprecht et al., 2021) and ENS^2 (Zhou et al., 2023) global-trained networks, which have been reported to outperform other methods on a wide array of benchmark tests.

We first examined the ability of our methods to estimate continuous changes in activity. Imputed spike predictions and ground truth spikes were smoothed with Gaussian filters of various widths. Even at low filter widths, our model predictions were tightly locked to true spike patterns for both excitatory and inhibitory classes (**Figure 4B, C**), as indicated by the higher correlations between our method predictions and ground truth at all filter widths, particularly at ten and twenty milliseconds. Results with CASCADE were not improved by training the network on the jGCaMP8f dataset itself (**Supplementary Figure 8**).

For discrete spike estimates, the older methods showed an offset (i.e. bias) of estimated spike time (**Figure 4B-E**) of 8.7 ± 59.1 ms (for CASCADE; median±estimated SD) or more, but $\text{Biophys}_{\text{SMC}}$ was relatively unbiased, with an average offset of -0.7 ± 9.2 ms (Figure 4E). The number of imputed spikes differed from ground truth by a median of 4 spikes per epoch for $\text{Biophys}_{\text{SMC}}$ 6 spikes per epoch for CASCADE, and 13-14 spikes per epoch for other methods. Our $\text{Biophys}_{\text{SMC}}$ method detected 5,831 imputed spikes, a 0.2% overestimate, comparable with the next-best method, CASCADE.

We quantified the timescale with which various methods could track changes in firing using the Pearson correlation between the time course of ground truth and that of the continuous probabilities for time-filtered data (**Figure 4D**). Pearson correlations of these predictions with ground truth spike times with different filtering time constants showed that $\text{Biophys}_{\text{SMC}}$ and $\text{Biophys}_{\text{ML}}$ outperformed other methods on all time scales for excitatory cells (repeated measures ANOVA, excitatory cells: p = 9e-25, n =37, Tukey HSD post hoc shows p < 0.01 for both Biophys methods compared to all others). The low number of inhibitory cells (three) did not allow their use in statistical comparisons.

Finally, we tested the ability of our methods to estimate individual spike times. On an epoch by epoch basis, the average time between imputed spikes and the nearest ground-truth spike (**Figure 4E**, left) was 6 ms for $\text{Biophys}_{\text{SMC}}$. $\text{Biophys}_{\text{SMC}}$ considerably outperformed the next-best unsupervised method, MLspike (uncertainty of 40 ms). In summary, for both cell types, the biophysical model-based methods outperformed all in-class and out-of-class alternatives.

Discussion

In this study, we identified and characterized nonlinear distortions in fluorescence signals from three fast GCaMP variants (GCaMP6f, jGCaMP7f, jGCaMP8f) arising from spike activity patterns. We discovered a novel use-dependent slowing of the fluorescence decay during periods of sustained activity. Using these empirical observations, we constructed a biophysical model which served as the foundation of an unsupervised ($\text{Biophys}_{\text{SMC}}$) and a supervised ($\text{Biophys}_{\text{ML}}$) spike inference method. These biophysically-based inference methods extracted spikes with greater precision than existing methods. The advantage of biophysical model-based approaches was most apparent under high-bandwidth conditions.

Our spike-decoding framework was composed of three basic parts. First, we made recordings in a minimal tissue-based system (acute slices) where paired fluorescent/spike recordings were as easy as possible to make. Second, we used in vitro recordings where all time-varying parameters of experiments were known precisely, save the GCaMP response itself. Finally, we used these recordings to jointly constrain models of the GCaMP response per se and to suggest an appropriate generative model of the cellular response.

Our study clarifies how response nonlinearities can differ between indicators. Earlier GCaMPs (6f and 7f) showed a facilitation-like nonlinearity in their fluorescence response lasting tens of milliseconds, amplifying signals from closely timed spikes as previously noted (Éltes et al., 2019; Wei et al., 2020; Huang et al., 2021; Schoenfeld et al., 2021). We found an additional, novel nonlinearity: a persistent use-dependence that builds progressively during periods of heightened activity. This second nonlinearity was particularly apparent for jGCaMP8f, whose half-decay responses were slowed by up to three-fold. We showed that this effect is problematic

for unsupervised methods that assume a linear mapping of spikes to fluorescence. In the linear SMC approach we used as a benchmark (PGBAR, (Diana et al., 2024)), elongated decay dynamics drove spurious predictions as the hysteretic effect forced the latent states to match the fluorescence dynamics (**Figure 3G, H**). This linear SMC, as well as MLspike (Deneux et al., 2016), were particularly poor spike predictors in the context of low SNR, high spike-rate data from inhibitory cells (**Figure 3H**; **Figure 4C**).

By leveraging a biophysically-based understanding of sensor behavior, we developed two complementary, high-performance spike inference methods. Initially, we applied the generative model directly within an unsupervised SMC framework to substantially improve accuracy, albeit with a computational cost inherent to Monte Carlo-based approaches (Vogelstein et al., 2010; Speiser et al., 2017). To address this limitation, we then used our biophysical model to produce large, synthetic datasets to train a supervised neural network that performed more quickly.

To our knowledge, our study is the first to report improvements in a machine learning training using a generative physical model approach. Because the biophysical model captures important features of GCaMP responses, we were able to use it as the engine for exploring how GCaMPs would react under different cellular and activity contexts. We achieved substantial improvements in spike time estimates by training our model on simulated spike patterns that explored a wide range of timing and patterns. The size and diversity of our training may explain why $\text{Biophys}_{\text{ML}}$ outperformed CASCADE trained on the jGCaMP8f data itself. While large, the jGCaMP8f excitatory cell dataset still falls within a range over which increasing training set size would be expected to improve performance (Rupprecht et al., 2021; Zhou et al., 2023). Indeed, limited training data is a fundamental hurdle for any machine learning approach, a problem that is particularly acute in the context of labor-intensive datasets such as paired optical/electrophysiology considered here.

However, training of supervised neural networks, even on extensive, heterogeneous datasets, was insufficient to guarantee accurate inference for sensors with previously unseen properties. Both ENS^2 and CASCADE, which rank highly on established benchmarks, exhibited temporal biases and overestimated rise times for jGCaMP8f (**Figure 4**). Notably, in contrast to a published report (Zhou et al., 2023), CASCADE outperformed ENS^2 on all aspects of inference in the jGCaMP8f dataset. This result highlights that observations made with neural networks trained on broad datasets do not generalize in instances where indicator properties differ substantially from those in the training dataset. Taken together, these results suggest that for both current and future calcium indicator proteins, building an effective supervised inference approach requires a thorough exploration of relevant dynamic regimes using either labor-intensive ground truth or the generative approach we describe here.

In summary, this study elucidates the biophysical mechanisms underlying GECI fluorescence responses and offers practical solutions for more accurate and reliable neural activity detection. As a final note, our approach may serve as a generalizable roadmap for linking fluorescence measurements to underlying neural activity. For example, the steps we introduce here are likely to generalize to other GECI variants—including red-shifted (Inoue et al., 2015, 2019; Dana et al., 2016) and chemigenetic sensors (Deo et al., 2021; Farrants et al., 2024). Appropriate state and sensor models may allow extension to other genetically encoded

sensors including those designed to detect neuromodulator release (e.g., Patriarchi et al., 2018; Sun et al., 2018) and voltage change (e.g., Evans et al., 2023; Platisa et al., 2023).

Methods

Animals. The following strains were used for physiological experiments: C57Bl/6J (Jackson Laboratories stock 000664); CB6F1 (BalbC and C57Bl/6J F1, source); and Gabra6 [B6;129P2-Gabra6tm2(cre)Wwis/Mmucd; source]. Both males and females were used and were between 40 and 130 days old. Animals were used in accordance with Princeton University's Institutional Animal Care and Use Committee and Institut Pasteur's CEEA-Paris1 approved protocols.

Protein Purification. GCaMP variants were cloned into the pET28b protein expression vector using GCaMP6f, 7f, and 7s backbones generously provided by Douglas Kim (Janelia) and Addgene (104488). Mutations were created through standard site-directed mutagenesis techniques. Plasmids were transformed into IPTG-inducible BL21(DE3) competent E. coli (MilliporeSigma 694504). Starter cultures of transformed cells were grown in 5 ml LB medium with 50 mg/L kanamycin at 37°C for 4 hours. Cultures were then added to 1 L LB medium with 50 mg/L kanamycin and grown at 37°C until the OD at 600 nm reached 1.0. 1 mM IPTG was added and the incubation temperature dropped to 25°C overnight for optimal protein expression.

Liquid cultures were centrifuged at 6K rcf for 10 minutes. Pellets were resuspended in 25 mM Tris-HCl, 500 mM NaCl, 20 mM imidazole, pH 8, with 1 mM PMSF for protease inhibition. Cells were mechanically lysed through an Emulsiflex homogenizer (ATA Scientific). Cell debris was removed through centrifugation at 13 K rcf for 45 minutes at 4°C and the supernatant bound to nickel-NTA agarose (ThermoScientific 25215). Protein was eluted with 25 mM Tris-HCl, 500 mM NaCl, 500 mM imidazole, pH 8. Proteins were further concentrated using 10 kDa MWCO centrifugal filters (MilliporeSigma UFC901008) and desalted (GE Healthcare 17085101) into 130 mM KMOPS (in mM:100 KCl, 30 MOPS, pH 7.2), or a buffer mimicking intracellular conditions (in mM: 125 KCl, 14.5 KOH, 30 NaCl, 0.7 Mg2Cl, 10 HEPES) termed internal buffer. Protein concentrations were determined by absorption spectrophotometry using alkali denaturation in 0.1M NaOH. Under these conditions, mature GCaMP chromophore exhibits a standard molar absorption coefficient of 44,000M-1cm-1 at 447 nm, allowing direct recovery of GCaMP concentration using Beer's law (Ward, 2005; Barnett et al., 2017).

Protein steady-state and kinetic characterization. Excitation and emission spectra were measured on a PTI Quantamaster 800 spectro-fluorometer (Horiba Jobin Yvon Inc., Edison, NJ, USA) with data collection under control of Felix GX software. For calcium-dependent fluorescence, steady-state measurements were made at 20 °C using 0.15 μM of purified protein suspended in zero-Ca2+ buffer or high-Ca2+ buffer from a calcium calibration kit (ThermoFisher C3008MP). The zero-Ca2+ buffer was reciprocally diluted with the high-Ca2+ buffer to reach free Ca2+ concentrations between 0.01 and 10 μM. Hill coefficient and Kd were estimated by fitting steady state data to the Hill equation.

The fluorometer was also used to prepare reagents for stopped-flow kinetic measurements. Nominally Ca2+-free buffers included KMOPS or internal buffer supplemented by 2 mM BAPTA (Invitrogen B1204). Increasing amounts of 1 M CaCl2 were added to create free calcium steps of 0 nM, 50 nM, and increasing by approximately 2x free calcium in ten steps

to 10 μM free calcium. Indicators were diluted to 175 nM in 0.1mM solution buffered by 0.1 mM BAPTA (see design considerations in **Supplementary Figure 2**).

Off-response kinetics buffers were designed to have a starting free calcium concentration of 10 μM in 100 μM BAPTA and a final nominal concentration of 0 nM or 50 nM free calcium when mixed to Ca2+-free buffer. Proteins were diluted to 35 nM in the 10 μM free calcium buffer. In all cases, Fura-2 (Molecular Probes F6799) and Fura-4F (Invitrogen F14174) were used to calibrate free calcium concentrations.

On-response and off-response kinetics were measured using an Applied Photophysics SX20 stopped-flow spectrometer. Excitation light was provided by a xenon arc lamp [type] directed through a monochromator set to a 4 nm passband centered on 480 nm, while emissions were collected through a 550 nm longpass filter (Newport FR-OG550). Dead time in the range of 0.6-1.5 ms was estimated by extrapolation from measurements using OGB-1 (Life Technologies, O6806). Measurements were made at 37°C with 60 μl per reaction chamber.

Adeno-associated virus constructs. Adeno-associated viruses (AAVs) were prepared by cloning the GCaMP variants into pAAV backbones (GenScript, Piscataway, NJ). Plasmids were incorporated into AAV serotype 1 (AAV2/1) and serotype DJ (AAV DJ) by the Princeton Neuroscience Institute Viral Neuroengineering Laboratory.

Stereotactic Viral Injection. Viral vectors were injected stereotactically into the cerebellar vermis. Mice were deeply anesthetized by intraperitoneal injections of 1.5%(Mérial) and 0.05% xylazine (Bayer). 2% Xylocaine (Newpharma) was applied to the cranial incision. 100 nl vermal injections (6.5 mm caudal to bregma, lateral 0.2 mm, ventral 3.6 mm and 3.4 mm) were infused over one minute. To allow for optimal transgene expression, mice were imaged 2 to 4 weeks after injection.

Slice Preparation. Animals were euthanized by rapid decapitation. The brains were quickly removed and placed in an ice-cold solution containing (in mM) 2.5 KCl, 0.5 CaCl2, 4 MgCl2, 1.25 NaH2PO4, 24 NaHCO3, 25 glucose, 230 sucrose, and 0.5 ascorbic acid. The buffer was bubbled with 95% O2 and 5% CO2. A Leica VT1200S vibratome was used to prepare coronal slices [thickness?], which were incubated at 32 °C for 30 min in (in mM): 85 NaCl, 2.5 KCl, 0.5 CaCl2, 4 MgCl2, 1.25 NaH2PO4, 24 NaHCO3, 25 glucose, 75 sucrose, and 0.5 ascorbic acid. The external recording solution contained (in mM) 125 NaCl, 2.5 KCl, 2.0 CaCl2, 1.0 MgCl2, 1.25 NaH2PO4, 25 NaHCO3, 25 glucose, and 0.5 ascorbic acid. Slices were maintained at room temperature for up to 6 h. All slice recordings were performed at 36–38°C.

Imaging in cerebellar brain slices. Parallel fiber boutons expressing fluorescent virus were imaged with an Ultima two-photon scanning scanhead (Bruker Nano Surfaces Division, Middleton, WI, USA) that was mounted on an Olympus BX61W1 microscope equipped with a water-immersion objective (60×/1.1-NA; Olympus Optical, Tokyo, Japan) and infrared Dodt-gradient contrast. Two-photon excitation was performed with a pulsed Ti:Sapphire laser (DeepSee, Spectra-Physics, France) tuned to 920 nm. Extracellular parallel fiber axonal stimulation was performed with a constant voltage stimulator (Digitimer Ltd, Letchworth Garden City, UK) and a patch pipette (typically with a tip resistance of 4–6 MΩ) filled with artificial cerebrospinal fluid and placed in the molecular layer adjacent to labeled parallel fibers. The fluorescence of single cerebellar granule cells was monitored using circular line scans along the cytoplasm of the GC somata or straight line scans across individual parallel fiber boutons.

Typical line rates were ~1 kHz. To determine threshold fluorescence, extracellular stimulation intensity was increased until clear fluorescence responses were observed after a train of 20–60 60-μs pulses at 100 or 300 Hz. To ensure action potential initiation for each stimulus pulse, the stimulus voltage was increased by 5 V above threshold.

Biophysical and cell models. We modeled GCaMP fluorescence as arising from semi-independent ("hemi-independent") (Lai et al., 2015) calcium binding at two lobes, each of which can subsequently bind a target peptide to become fluorescent. Formally, each lobe transitions between an unbound and a calcium-bound state, which is governed by first-order binding and unbinding reactions:

$$\frac{d(\mathrm{bound_{lobe}})}{dt} = k_{\mathrm{on,lobe}}\,\mathrm{unbound_{lobe}} - k_{\mathrm{off,lobe}}\,\mathrm{bound_{lobe}} \qquad \text{eqn. 1}$$

where $k_{\mathrm{on,lobe}}$ and $k_{\mathrm{off,lobe}}$ are rate constants for binding and unbinding at each lobe. We defined:

$$k_{\mathrm{on,lobe}} = \frac{k_{\mathrm{off,lobe}}}{\left(K_{a,\mathrm{lobe}}\right)^{H_{\mathrm{lobe}}}} \qquad \text{eqn. 2}$$

where $K_{a,\mathrm{lobe}}$ is an apparent dissociation constant and H_{lobe} is a Hill coefficient describing cooperative binding. Once a lobe is bound with calcium, it can transition to a fluorescent state by binding the target peptide. This step similarly follows first-order kinetics:

$$\frac{d(\mathrm{fluorescent})}{dt} = k_{\mathrm{on,peptide,lobe}}\,\mathrm{bound_{lobe}} - k_{\mathrm{off,peptide,lobe}}\,\mathrm{fluorescent} \qquad \text{eqn. 3}$$

All fluorescent states (i.e., those in which a lobe is calcium-bound and has the peptide bound) contribute equally to total fluorescence. For stopped-flow simulations, model fluorescence was normalized between 0 (occupancy of fluorescent states at zero calcium) and 1 (occupancy at saturating calcium). For cell-based simulations, fluorescence was scaled to a dimensionless quantity F by setting to 1 at 0 calcium and the parameter R_f – the dynamic range of the indicator – at saturating calcium level. $\frac{\Delta F}{F}$ was then calculated as:

$$\frac{\Delta F}{F} = \frac{F\left(\mathrm{Ca_{current}}\right) - F\left(\mathrm{Ca_{basal}}\right)}{F\left(\mathrm{Ca_{basal}}\right)} \qquad \text{eqn. 4}$$

where $F(\mathrm{Ca_{current}})$ is the instantaneous normalized fluorescence at the current free-calcium level, and $F(\mathrm{Ca_{basal}})$ is the steady-state fluorescence at basal calcium.

To simulate intracellular calcium transients (e.g., after action potentials), we extended the model from Rebola et al. 2019 (Rebola et al., 2019) by including an internal calcium

reservoir with influx and efflux governed by Michaelis–Menten dynamics. Because cerebellar granule cells have fast, low affinity endogenous buffers expressed at high concentrations, we linearized the buffer's binding capacity κ_B (Neher and Augustine, 1992) to reduce computational cost. Specifically, each small increment of free calcium $\mathrm{Ca_{in}}$ is instantly equilibrated with endogenous buffer:

$$\frac{d(\mathrm{BCa})}{dt} = \frac{\mathrm{Ca_{in}}\ \kappa_B}{\kappa_B + 1} \qquad \text{eqn. 5}$$

where BCa is the portion of endogenous buffer bound to calcium, a ratio of approximately 40 for our standard granule cell model. This linearization preserves the overall calcium balance while allowing faster numerical integration of high buffer concentration simulations.

For obtaining full GCaMP model parameterization we globally fit all traces obtained from stopped flow for each variant by gradient descent from 1500 quasi-randomly selected initial points in parameter space. GCaMP parameters from each run were then fixed and best fits were obtained across our ex vivo datasets by gradient descent over cell-specific parameters. The GCaMP model parameters which minimized errors across experimental contexts were then selected and fixed for each GCaMP variant.

Bayesian and machine-learning spike inference algorithms. In order to infer spike times from fluorescence time series using the biophysical model of jGCaMP8f described in the main text we adopted the Bayesian framework developed by Diana et al, 2024 based on sequential Monte Carlo methods (particle Gibbs with ancestor sampling, PGAS, (Diana et al., 2024)) which enabled us to estimate simultaneously the posterior distributions of spike times and the parameters of the cell model, including the GCaMP concentration, calcium extrusion rates, peak amplitude of the calcium flux due to single action potentials and the dynamic range of the probe. Single point estimates of model parameters and spike times were obtained by using maximum-a-posteriori estimates.

We compared the performance of our method with MLspike (Deneux et al., 2016) which employs a different model for the calcium indicator dynamics and baseline fluorescence. Spike inference in MLspike is carried out by discretizing all continuous dynamical variables in the model and applying the Viterbi algorithm to extract maximum-a-posteriori estimates of spike times. One of the weaknesses of this approach is the difficulty of estimating the model parameters, for which Deneux et al provide ad hoc calibration schemes. We directly addressed this issue using the PGAS sampling algorithm.

We compared our method with state-of-the-art supervised machine-learning models: CASCADE (Rupprecht et al., 2021) and ENS^2 (Zhou et al., 2023). The two approaches use different network architectures. CASCADE returns the spike probability at each time point by taking as input a local time window by using a trained convolutional network while ENS^2 uses the U-net applied on fixed-length segments of the original calcium trace.

Average spike time error within 8-s epochs (per-epoch error, PE) (Figure 4E) was converted to individual spike-time error using the formula PE sqrt(N), where N is the number of spikes in that epoch.

Statistics. Across figures, box and whisker plots comprise a box indicating the median and 25-75th percentile range and whiskers indicating the shorter of 1.5 times the interquartile range or the extreme data point.

References

Akerboom J et al. (2012) Optimization of a GCaMP calcium indicator for neural activity imaging. J Neurosci Off J Soc Neurosci 32:13819–13840.

Badura A, Sun XR, Giovannucci A, Lynch LA, Wang SSH (2014) Fast calcium sensor proteins for monitoring neural activity. Neurophotonics 1:025008.

Barnett LM, Hughes TE, Drobizhev M (2017) Deciphering the molecular mechanism responsible for GCaMP6m's Ca2+-dependent change in fluorescence. PLOS ONE 12:e0170934.

Brown SE, Martin SR, Bayley PM (1997) Kinetic Control of the Dissociation Pathway of Calmodulin-Peptide Complexes*. J Biol Chem 272:3389–3397.

Chen T-W, Wardill TJ, Sun Y, Pulver SR, Renninger SL, Baohan A, Schreiter ER, Kerr RA, Orger MB, Jayaraman V, Looger LL, Svoboda K, Kim DS (2013) Ultrasensitive fluorescent proteins for imaging neuronal activity. Nature 499:295–300.

Dana H, Mohar B, Sun Y, Narayan S, Gordus A, Hasseman JP, Tsegaye G, Holt GT, Hu A, Walpita D, Patel R, Macklin JJ, Bargmann CI, Ahrens MB, Schreiter ER, Jayaraman V, Looger LL, Svoboda K, Kim DS (2016) Sensitive red protein calcium indicators for imaging neural activity. eLife 5:e12727.

Dana H, Sun Y, Mohar B, Hulse BK, Kerlin AM, Hasseman JP, Tsegaye G, Tsang A, Wong A, Patel R, Macklin JJ, Chen Y, Konnerth A, Jayaraman V, Looger LL, Schreiter ER, Svoboda K, Kim DS (2019) High-performance calcium sensors for imaging activity in neuronal populations and microcompartments. Nat Methods 16:649–657.

Demas J, Manley J, Tejera F, Kim H, Traub FM, Chen B, Vaziri A (2021) High-Speed, Cortex-Wide Volumetric Recording of Neuroactivity at Cellular Resolution using Light Beads Microscopy. bioRxiv:2021.02.21.432164.

Deneux T, Kaszas A, Szalay G, Katona G, Lakner T, Grinvald A, Rózsa B, Vanzetta I (2016) Accurate spike estimation from noisy calcium signals for ultrafast three-dimensional imaging of large neuronal populations in vivo. Nat Commun 7:12190.

Deo C, Abdelfattah AS, Bhargava HK, Berro AJ, Falco N, Farrants H, Moeyaert B, Chupanova M, Lavis LD, Schreiter ER (2021) The HaloTag as a general scaffold for far-red tunable chemigenetic indicators. Nat Chem Biol 17:718–723.

Diana G, Sermet BS, DiGregorio DA (2024) High frequency spike inference with particle Gibbs sampling. eLife 13 Available at: https://elifesciences.org/reviewed-preprints/94723 [Accessed September 18, 2024].

DiGregorio DA, Peskoff A, Vergara JL (1999) Measurement of Action Potential-Induced Presynaptic Calcium Domains at a Cultured Neuromuscular Junction. J Neurosci 19:7846–7859.

Éltes T, Szoboszlay M, Kerti-Szigeti K, Nusser Z (2019) Improved spike inference accuracy by estimating the peak amplitude of unitary [Ca2+] transients in weakly GCaMP6f-expressing hippocampal pyramidal cells. J Physiol 597:2925–2947.

Evans SW et al. (2023) A positively tuned voltage indicator for extended electrical recordings in the brain. Nat Methods 20:1104–1113.

Faas GC, Raghavachari S, Lisman JE, Mody I (2011) Calmodulin as a direct detector of Ca2+ signals. Nat Neurosci 14:301–304.

Farrants H et al. (2024) A modular chemigenetic calcium indicator for multiplexed in vivo functional imaging. Nat Methods 21:1916–1925.

Friedrich J, Zhou P, Paninski L (2017) Fast online deconvolution of calcium imaging data. PLOS Comput Biol 13:e1005423.
Huang L, Ledochowitsch P, Knoblich U, Lecoq J, Murphy GJ, Reid RC, de Vries SE, Koch C, Zeng H, Buice MA, Waters J, Li L (2021) Relationship between simultaneously recorded spiking activity and fluorescence signal in GCaMP6 transgenic mice Westbrook GL, Svoboda K, Higley M, Sabatini BL, eds. eLife 10:e51675.
Inoue M et al. (2019) Rational Engineering of XCaMPs, a Multicolor GECI Suite for In Vivo Imaging of Complex Brain Circuit Dynamics. Cell 177:1346-1360.e24.
Inoue M, Takeuchi A, Horigane S, Ohkura M, Gengyo-Ando K, Fujii H, Kamijo S, Takemoto-Kimura S, Kano M, Nakai J, Kitamura K, Bito H (2015) Rational design of a high-affinity, fast, red calcium indicator R-CaMP2. Nat Methods 12:64–70.
Johnson JD, Snyder C, Walsh M, Flynn M (1996) Effects of Myosin Light Chain Kinase and Peptides on Ca2+ Exchange with the N- and C-terminal Ca2+ Binding Sites of Calmodulin (∗). J Biol Chem 271:761–767.
Lai M, Brun D, Edelstein SJ, Novère NL (2015) Modulation of Calmodulin Lobes by Different Targets: An Allosteric Model with Hemiconcerted Conformational Transitions. PLOS Comput Biol 11:e1004063.
Li P, Geng X, Jiang H, Caccavano A, Vicini S, Wu J (2019) Measuring Sharp Waves and Oscillatory Population Activity With the Genetically Encoded Calcium Indicator GCaMP6f. Front Cell Neurosci 13 Available at: https://www.frontiersin.org/journals/cellular-neuroscience/articles/10.3389/fncel.2019.00274/full [Accessed December 30, 2024].
Linse S, Helmersson A, Forsén S (1991) Calcium binding to calmodulin and its globular domains. J Biol Chem 266:8050–8054.
Pachitariu M, Stringer C, Harris KD (2018) Robustness of Spike Deconvolution for Neuronal Calcium Imaging. J Neurosci 38:7976–7985.
Patriarchi T, Cho JR, Merten K, Howe MW, Marley A, Xiong W-H, Folk RW, Broussard GJ, Liang R, Jang MJ, Zhong H, Dombeck D, Zastrow M von, Nimmerjahn A, Gradinaru V, Williams JT, Tian L (2018) Ultrafast neuronal imaging of dopamine dynamics with designed genetically encoded sensors. Science 360 Available at: https://science.sciencemag.org/content/360/6396/eaat4422 [Accessed April 12, 2021].
Platisa J, Ye X, Ahrens AM, Liu C, Chen IA, Davison IG, Tian L, Pieribone VA, Chen JL (2023) High-speed low-light in vivo two-photon voltage imaging of large neuronal populations. Nat Methods 20:1095.
Pnevmatikakis EA, Merel J, Pakman A, Paninski L (2013) Bayesian spike inference from calcium imaging data. Available at: http://arxiv.org/abs/1311.6864 [Accessed December 30, 2024].
Rebola N, Reva M, Kirizs T, Szoboszlay M, Lőrincz A, Moneron G, Nusser Z, DiGregorio DA (2019) Distinct Nanoscale Calcium Channel and Synaptic Vesicle Topographies Contribute to the Diversity of Synaptic Function. Neuron 104:693-710.e9.
Regehr WG, Atluri PP (1995) Calcium transients in cerebellar granule cell presynaptic terminals. Biophys J 68:2156–2170.
Rose T, Goltstein PM, Portugues R, Griesbeck O (2014) Putting a finishing touch on GECIs. Front Mol Neurosci 7 Available at: https://www.frontiersin.org/articles/10.3389/fnmol.2014.00088/full#B17 [Accessed June 25, 2021].
Rupprecht P, Carta S, Hoffmann A, Echizen M, Blot A, Kwan AC, Dan Y, Hofer SB, Kitamura K, Helmchen F, Friedrich RW (2021) A database and deep learning toolbox for noise-optimized, generalized spike inference from calcium imaging. Nat Neurosci 24:1324–1337.
Sabatini BL, Regehr WG (1998) Optical measurement of presynaptic calcium currents. Biophys

J 74:1549–1563.
Sariyildiz MB, Kalantidis Y, Alahari K, Larlus D (2023) No Reason for No Supervision: Improved Generalization in Supervised Models. Available at: http://arxiv.org/abs/2206.15369 [Accessed December 31, 2024].
Schoenfeld G, Carta S, Rupprecht P, Ayaz A, Helmchen F (2021) In Vivo Calcium Imaging of CA3 Pyramidal Neuron Populations in Adult Mouse Hippocampus. eNeuro 8 Available at: https://www.eneuro.org/content/8/4/ENEURO.0023-21.2021 [Accessed October 16, 2024].
Sebastian J, Mari Ganesh Kumar M, Sreekar YS, Rikhye RV, Sur M, Murthy HA (2017) GDspike: An accurate spike estimation algorithm from noisy calcium fluorescence signals. 2017 IEEE Int Conf Acoust Speech Signal Process ICASSP:1043–1047.
Seroussi I, Zeitouni O (2022) Lower Bounds on the Generalization Error of Nonlinear Learning Models. Available at: http://arxiv.org/abs/2103.14723 [Accessed December 31, 2024].
Speiser A, Yan J, Archer EW, Buesing L, Turaga SC, Macke JH (2017) Fast amortized inference of neural activity from calcium imaging data with variational autoencoders. In: Advances in Neural Information Processing Systems. Curran Associates, Inc. Available at: https://papers.nips.cc/paper_files/paper/2017/hash/5d6646aad9bcc0be55b2c82f69750387-Abstract.html [Accessed December 18, 2024].
Sun F et al. (2018) A Genetically Encoded Fluorescent Sensor Enables Rapid and Specific Detection of Dopamine in Flies, Fish, and Mice. Cell 174:481-496.e19.
Sun XR, Badura A, Pacheco DA, Lynch LA, Schneider ER, Taylor MP, Hogue IB, Enquist LW, Murthy M, Wang SS-H (2013) Fast GCaMPs for improved tracking of neuronal activity. Nat Commun 4:2170.
Tian L, Hires SA, Mao T, Huber D, Chiappe ME, Chalasani SH, Petreanu L, Akerboom J, McKinney SA, Schreiter ER, Bargmann CI, Jayaraman V, Svoboda K, Looger LL (2009) Imaging neural activity in worms, flies and mice with improved GCaMP calcium indicators. Nat Methods 6:875.
Vogelstein JT, Packer AM, Machado TA, Sippy T, Babadi B, Yuste R, Paninski L (2010) Fast Nonnegative Deconvolution for Spike Train Inference From Population Calcium Imaging. J Neurophysiol 104:3691–3704.
Ward WW (2005) Biochemical and Physical Properties of Green Fluorescent Protein. In: Green Fluorescent Protein, pp 39–65. John Wiley & Sons, Ltd. Available at: https://onlinelibrary.wiley.com/doi/abs/10.1002/0471739499.ch3 [Accessed December 30, 2024].
Wei Z, Lin B-J, Chen T-W, Daie K, Svoboda K, Druckmann S (2020) A comparison of neuronal population dynamics measured with calcium imaging and electrophysiology. PLOS Comput Biol 16:e1008198.
Xiao D, Vanni MP, Mitelut CC, Chan AW, LeDue JM, Xie Y, Chen AC, Swindale NV, Murphy TH (2017) Mapping cortical mesoscopic networks of single spiking cortical or sub-cortical neurons Kleinfeld D, ed. eLife 6:e19976.
Zhang Y et al. (2023) Fast and sensitive GCaMP calcium indicators for imaging neural populations. Nature 615:884–891.
Zhou Z, Yip HM, Tsimring K, Sur M, Ip JPK, Tin C (2023) Effective and efficient neural networks for spike inference from in vivo calcium imaging. Cell Rep Methods 3:100462.

Main Figure Legends

Figure 1 | Nonlinear response characteristics of fast GCaMPs in a controlled, ex vivo setting. (**A**) Schematic of experimental approach showing sites of extracellular stimulation and imaged regions (highlighted in yellow). (**B**) Representative traces obtained across sensors for single spike response, with mean overlaid to single trial response. (**C**) Traces from B averaged and normalized to demonstrate kinetic properties of GCaMPs compared to the low affinity synthetic indicator, OGB-5N. (**D-F**) Peak response amplitude, signal-to-noise ratio, and 10-90% rise time for individual boutons. Each symbol is averaged across trials. (**G**) averaged responses to one stimulus or two stimuli spaced 10 ms apart. (**H**) Relative amplitude of responses to a second stimulus spaced at various time intervals from the first stimulus. Each point represents an average of stimuli for one bouton. (**I**) Responses to 1 stimulus (left), 10 stimuli at 100 Hz overlaid to the single stimulus response (center), and normalized to the amplitude of a single-stimulus response to demonstrate prolonged decay (right). (**J**) Half-decay times as a function of stimulus number. (**K-L**) Convolution of a single-stimulus response with the times of stimuli to demonstrate effect of short-term amplitude non-linearity in GCaMP6f responses in K and cumulative signal arising from many stimuli for jGCaMP8f in L. Stars indicate statistical significance as: *$p<0.05$, **$p<0.01$, ***$p<0.001$.

Figure 2 | Stopped-flow fluorimetry of GCaMP dynamic responses. (**A**) Schematic of stopped-flow experiment and rising steps of calcium concentration. (**B**) Step-down protocols for decreasing calcium. (**C**) Responses to steps up from 0 μM free calcium. (**D**) Responses to steps down from 10 μM free calcium. (**E**) Half-rise times for GCaMP6f, jGCaMP7f, and jGCaMP8f as a function of calcium step size. Shaded gray region indicates the physiological range of intracellular signals. (**F**) Comparison of brain slice presynaptic bouton signals with stopped-flow rise times for the three indicator variants. (**G**) Rising phase responses on logarithmic time scales. Symbols indicate the time points plotted in (**H**). (**H**) Hill plots of rising and steady-state responses to steps in calcium. Colored numbers at the plot margins indicate Hill coefficients. (**I**) Comparison of brain slice amplitude nonlinearity at 10 ms inter-stimulus response with respect to Hill coefficients. (**J**) Representative stopped-flow traces with y-axis values presented on a log scale for jGCaMP8f (left) and GCaMP6f (right). Sums of exponentials for each indicator demonstrate the biphasic response and the greater contrast in speed of kinetic components seen in jGCaMP8f. (**K**) Quantification of the factor of slowing seen in GCaMP fluorescence decay in response to 1 and 10 stimuli in brain slices. (**L**) Comparison of brain slice slowing to accessible slowing (see main text and methods). Error bars in all panels represent the interquartile range of the distribution.

Figure 3 | A biophysical model for GCaMP response. (**A**) Schematic GCaMP model depicting key pathways to fluorescence as well as states highlighted in analyses of the model which were reached via fast N-lobe and slow C-lobe-based rate constants. (**B**) Schematic diagram of physiological response of a cellular structure containing endogenous calcium buffer, GCaMP, and intracellular and plasma membrane calcium extrusion (pump) mechanisms. (**C**) Fits of the GCaMP model to the three GCaMP variants with different parameters for each variant. (**D**) Fits of the cell model to physiological data with fixed GCaMP model parameters.

Vertical lines indicate action potential (spike) times. (**E**) Occupancy of the fast-fluorescent, slow-fluorescent, and slow non-fluorescent states of GCaMP indicating a mechanism for use-dependent slowing of fluorescence decay, becoming most apparent after 10 action potentials. (**F**) Predictions on simulated ground-truth data for an excitatory neuron. The data consists of a single spike (black) or a 10 Hz Poisson train of spikes (gray) (top panel). Lower panels show the average posterior spike probability (solid lines) and spikes times from a single trajectory (triangles) derived by our SMC method employing either the biophysical model ($\text{Biophys}_{\text{SMC}}$, green) or a linear model ($\text{Linear}_{\text{SMC}}$, pink) as its generative engine. Vertical lines indicate action potential (spike) times. (**G**) As in (**F**) with simulated ground truth for an inhibitory cell.

Figure 4: Improved action potential inference from generative model-based methods. (**A**) A generative model for imputing action potential times based on iterative fitting. The biophysical GCaMP model was held fixed while cell parameters were varied. Responses to action potential sequences were generated to fit cell parameters ($\text{Biophys}_{\text{SMC}}$). After fitting was complete, the $\text{Biophys}_{\text{SMC}}$ model was then used to train a machine learning based model. (**B, C**) Imputed spike probabilities using a variety of unsupervised and supervised models. Values of r indicate Pearson correlation between the time course of ground truth and that of the imputed probabilities for data filtered at 20 ms. Vertical lines indicate true spike times and tick marks indicate imputed spikes. (**B**) shows data from an excitatory cell while (**C**) shows data from an inhibitory cell. (**D**) Pearson correlations for different filtering time constants. (**E**) Discrete spike estimate statistics. Left panels shows the average time between the nearest imputed and ground truth spikes while the right shows the normalized number of spikes that were over or underestimated. Individual points are calculated over 8-second epochs covering 1000 data points randomly selected from the full dataset.(**E**) Timing and detection accuracy of the different imputation models. Left, distribution of average across-epoch error for the various methods. Each point indicates the average signed error for a single epoch. Smoothed histograms and box/whisker plots summarize all errors. Right, spike number bias with less than 1 indicating underestimate, and over 1 indicating overestimate of the true spike number.

Supplementary Figure Legends

Supplementary Figure 1 | jGCaMP8f response decay is captured by two kinetic components. (**A**) Representative boutons response to 1, 2, and 10 stimuli overlaid and aligned by first stimulus time. (**B**) Responses normalized and aligned to last spike. (**C**) Example fits to dual sums of exponentials showing fast and slow components of decay. (**D**) Dependence of fast (top) and slow (middle) time constants on the number of stimuli, and relative contribution of the slow component (τ_2) to the overall time course (bottom). Individual bouton values shown as low linewidth traces with group means shown as thicker line and SEM as error bars, *n* = 6 boutons and 3 granule cell somata.

Supplementary Figure 2 | The impact of calcium clamp design on observed stopped-flow dynamics. (**A-B**) Schematic of stopped-flow buffer systems using (**A**) a slow buffer (EGTA) and containing unbuffered calcium in the calcium-containing bolus (**A**) and (**B**) a system with a fast buffer (BAPTA) and fully buffered calcium in the calcium-containing bolus. (**C**) Simulations of the EGTA-based system presented in (**A**) show uncontrolled free calcium concentrations in the first few milliseconds of large calcium steps, but (**D**) BAPTA-based experiments do not. (**E**) Measurements of OGB-1 responses (left) reflect uncontrolled responses that are matched by simulations of the buffer system (right). (**F**) OGB-1 data and simulations in BAPTA-based buffers. (**G**) Artifactual fast on-response to jGCaMP8f in EGTA-based buffer system. (**H**) True jGCaMP8f response in BAPTA-based buffer system.

Supplementary Figure 3 | Magnesium affects the properties of jGCaMP8f much more than older GCaMPs. (**A**) Emission spectra of GCaMP variants in standard protein purification buffer (KMOPS, left) and under intracellular conditions that include magnesium (2 mM Mg^{2+}). (**B**) Fluorimeter counts at 490 nm under calcium-free (left) or saturating calcium (right) conditions. jGCaMP8f, but not other variants, shows strong magnesium-dependence of fluorescence emission under low-calcium conditions. No indicator shows this effect at saturating calcium. (**C**) Quantification of the weak dependence of GECI dynamic range R_f (saturating calcium divided by calcium-free fluorescence output) on temperature (left) or ionic strength (center) compared to the effect seen with magnesium (right). (**D**) Dynamic range of GCaMP variants at mammalian near-physiological conditions. (**E**) Schematic of stopped-flow experiment to measure responses to rising steps of calcium concentration. (**F**) Half-rise times to calcium steps are accelerated most by magnesium for jGCaMP8f, less so for GCaMP6f, and not for jGCaMP7f.

Supplementary Figure 4 | Biphasic responses of GCaMPs to increasing calcium steps. (**A**) Schematic of stopped-flow experiment and rising calcium-step protocol. (**B**) Example analysis of fit to a sum of two exponentials. (**C**) Monoexponential rising kinetics for Oregon Green BAPTA-1 (OGB-1) and biexponential kinetics for GCaMP variants. (**D**) Dependence of fast and slow components on amplitude of calcium step. Upper plots show rate constants represented in the response at the indicated step. In the lower plots, vertical bars show relative amplitude of fast (dark) and slow (light) components. (**E**) Schematic of decreasing-calcium step protocol. (**F**) Fluorescence responses to decreasing calcium steps. (**G**) Breakdown of kinetic components contributing to the decay of fluorescence as in (**D**). Due to the low number of steps

considered, analysis for all variants is included in this single plot. (**H**) Monoexponential decay for OGB-1 and more complex responses for GCaMP variants.

Supplementary Figure 5 | Selection of GCaMP biophysical parameters using in vitro and ex vivo datasets. (**A**) Distributions of parameters on fits from randomized seeds with GCaMP model parameters at figure left and residuals from best fits to stopped-flow and ex vivo experiments (paired pulse, 1-2-10 pulse, and Poisson train) based on optimizing cell parameters. GCaMP parameter sets were sorted by hierarchical clustering and then by lowest summed residuals within each cluster. This procedure allowed qualitative assessment of parameters that lay in different local minima of the parameter space. (**B**) Fitted data examples for cluster 1, which was used for all further modeling. (**C**) Fitted data for cluster 5. (**D**) Fitted data for cluster 9. In paired-pulse and Poisson train data, vertical lines indicate the times of action potentials. Expanded timescale of Poisson responses at right. Neither cluster 5 or 9 captured the differential slowing across the Poisson responses.

Supplementary Figure 6 | A full biophysical state analysis of GCaMP response. (**A**) Full biophysical state model of GCaMP response. Specific states referred to as “fast fluorescent”, “slow fluorescent”, and “slow, non-fluorescent” have centers color-coded as in model state traces below. (**B**) Best-fit parameter values for GCaMP6f, jGCaMP7f, and jGCaMP8f. (**C**) Model fits to 0.5 μM increasing step of calcium (top), with model state broken down by occupancy. Note that jGCaMP8f is distinguished by its near-exclusive use of the fast fluorescent states. (**D**) As in (**C**) for decreasing step. jGCaMP8f is distinguished by fast, persistent entry into the slow, non-fluorescent state. (**E**) Model fits to fluorescence responses in presynaptic boutons of granule cells. (**F**) State occupancy for the fluorescence responses shown in (**E**). Fast responses arise in part from high occupancy of a slow, non-fluorescent state at basal calcium for jGCaMP8f which efficiently transitions to fluorescence on elevation of calcium.

Supplementary Figure 7 | Generative cell-based model of fluorescence time series. Graphical representation of the generative SMC model described in the main text. White circles denote unknown variables, gray circles denote measurements and bare variables are fixed prior hyperparameters. Plates denote groups of variables. Note that GCaMP model parameters are included, but fixed for the SMC approach.

Supplementary Figure 8 | Training on jGCaMP8f data does not improve CASCADE performance. (**A**) Imputed spike probabilities using the CASCADE Global Exc model or one trained on the jGCaMP8f dataset itself. Values of r indicate Pearson correlation between the time course of ground truth and that of the imputed probabilities for data filtered at 20 ms. Vertical lines indicate true spike times and tick marks indicate imputed spikes. (**B**) Pearson correlations for different filtering time constants.

Figure 1

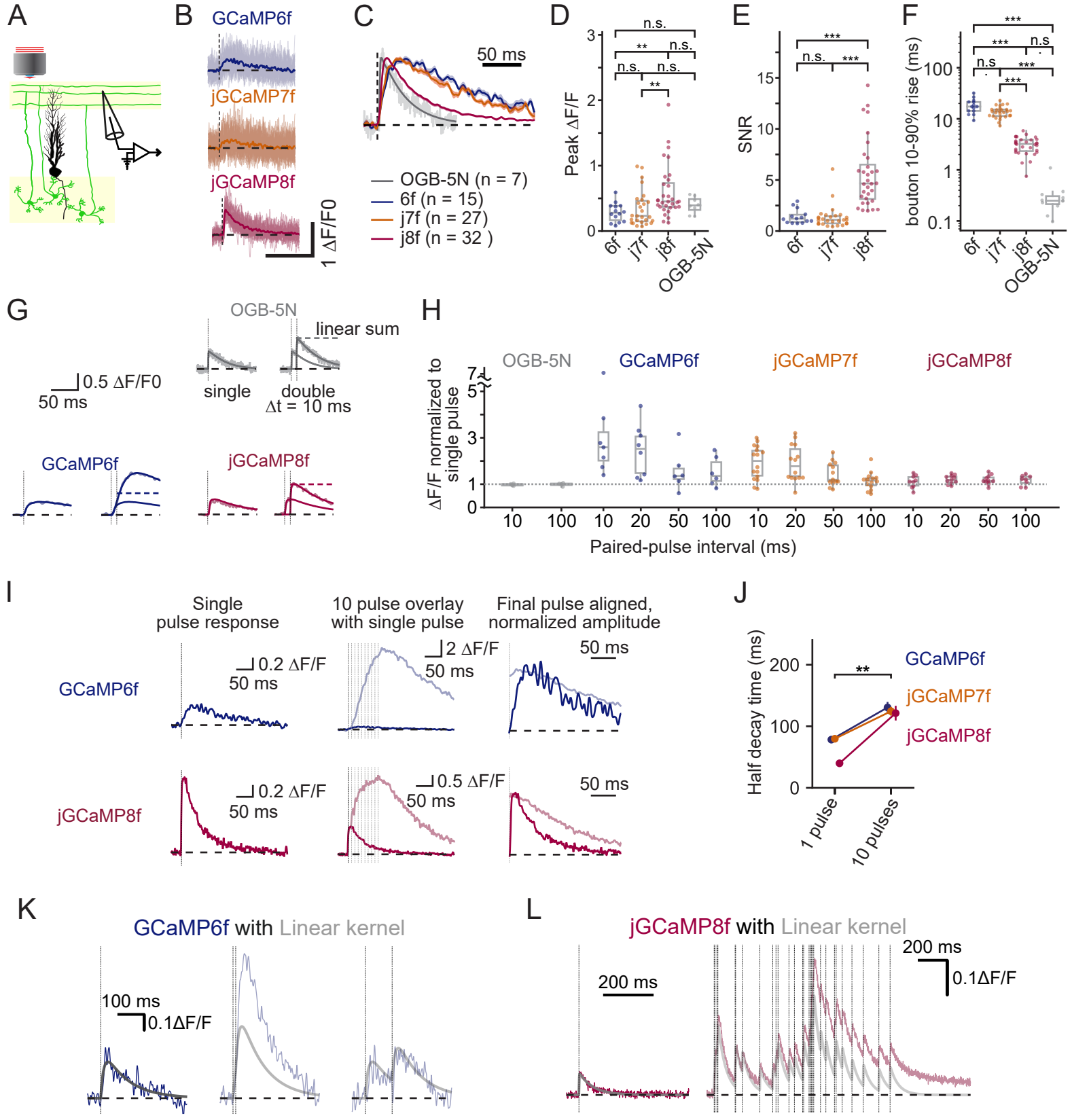
A
B
GCaMP6f
jGCaMP7f
jGCaMP8f
1 ΔF/F0
C
50 ms
OGB-5N (n = 7)
6f (n = 15)
j7f (n = 27)
j8f (n = 32)
D
Peak ΔF/F
n.s.
**
n.s.
n.s.
n.s.
**
6f
j7f
j8f
OGB-5N
E
SNR
***
n.s.
***
6f
j7f
j8f
F
bouton 10-90% rise (ms)
***
***
n.s
n.s
***
***
6f
j7f
j8f
OGB-5N
G
OGB-5N
linear sum
0.5 ΔF/F0
50 ms
single
double
Δt = 10 ms
GCaMP6f
jGCaMP8f
H
OGB-5N
GCaMP6f
jGCaMP7f
jGCaMP8f
ΔF/F normalized to single pulse
Paired-pulse interval (ms)
I
Single pulse response
10 pulse overlay with single pulse
Final pulse aligned, normalized amplitude
GCaMP6f
0.2 ΔF/F
50 ms
2 ΔF/F
50 ms
50 ms
jGCaMP8f
0.2 ΔF/F
50 ms
0.5 ΔF/F
50 ms
50 ms
J
Half decay time (ms)
**
GCaMP6f
jGCaMP7f
jGCaMP8f
1 pulse
10 pulses
K
GCaMP6f with Linear kernel
100 ms
0.1ΔF/F
L
jGCaMP8f with Linear kernel
200 ms
200 ms
0.1ΔF/F

Figure 2

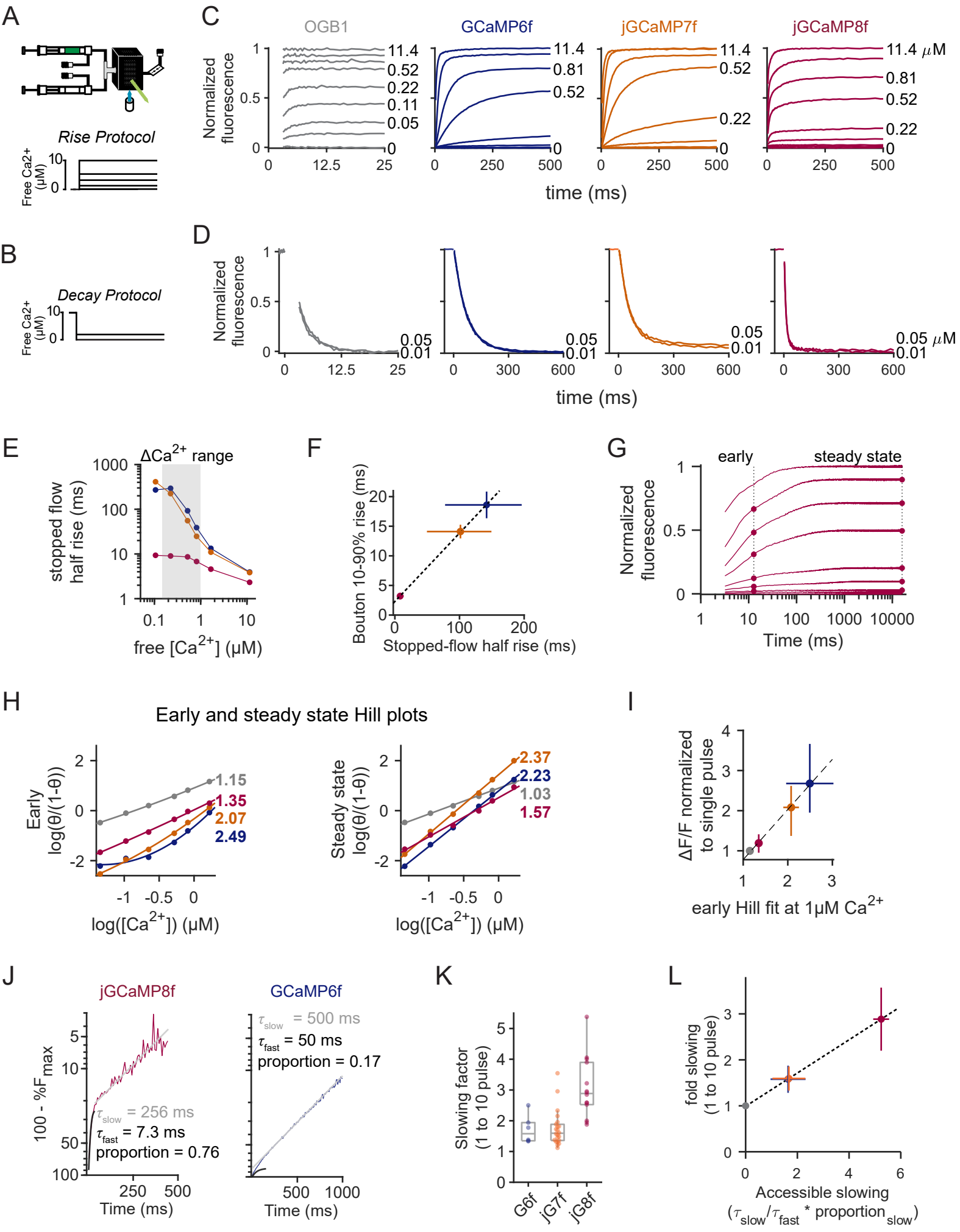
A
Rise Protocol
Free Ca2+ (μM)
10
0
B
Decay Protocol
Free Ca2+ (μM)
10
0
C
OGB1
GCaMP6f
jGCaMP7f
jGCaMP8f
Normalized fluorescence
11.4
0.52
0.22
0.11
0.05
0
11.4
0.81
0.52
0
11.4
0.52
0.22
0
11.4 μM
0.81
0.52
0.22
0
time (ms)
D
Normalized fluorescence
0.05
0.01
0.05
0.01
0.05
0.01
0.05 μM
0.01
time (ms)
E
ΔCa2+ range
stopped flow half rise (ms)
free [Ca2+] (μM)
F
Bouton 10-90% rise (ms)
Stopped-flow half rise (ms)
G
early
steady state
Normalized fluorescence
Time (ms)
H
Early and steady state Hill plots
Early log(θ/(1-θ))
1.15
1.35
2.07
2.49
log([Ca2+]) (μM)
Steady state log(θ/(1-θ))
2.37
2.23
1.03
1.57
log([Ca2+]) (μM)
I
ΔF/F normalized to single pulse
early Hill fit at 1μM Ca2+
J
jGCaMP8f
100 - %Fmax
τslow = 256 ms
τfast = 7.3 ms
proportion = 0.76
Time (ms)
GCaMP6f
τslow = 500 ms
τfast = 50 ms
proportion = 0.17
Time (ms)
K
Slowing factor (1 to 10 pulse)
G6f
jG7f
jG8f
L
fold slowing (1 to 10 pulse)
Accessible slowing
(τslow/τfast * proportionslow)

Figure 3

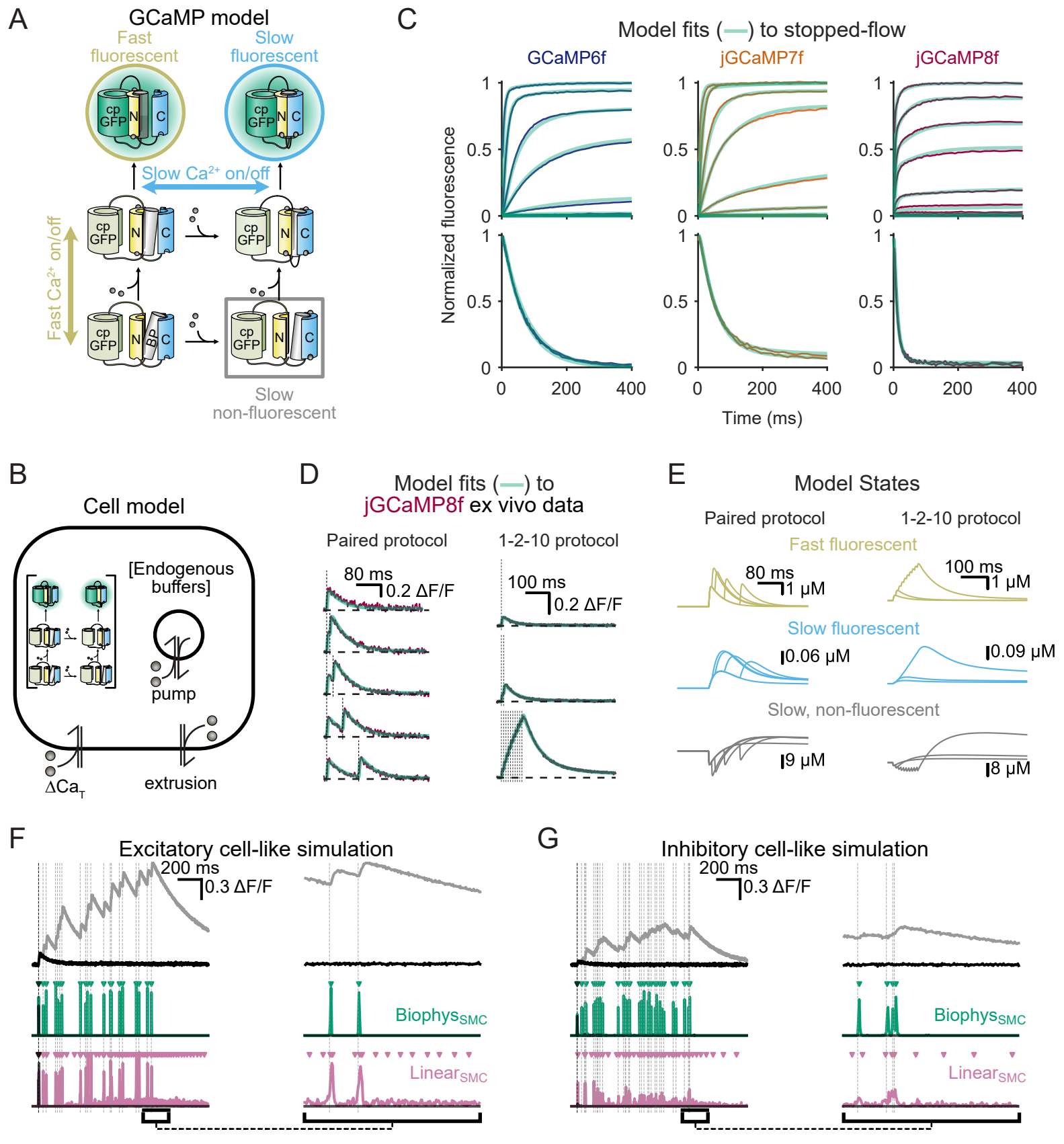
A
GCaMP model
Fast fluorescent
Slow fluorescent
cp GFP
N
C
Slow Ca2+ on/off
Fast Ca2+ on/off
Slow non-fluorescent
B
Cell model
[Endogenous buffers]
pump
ΔCaT
extrusion
C
Model fits (—) to stopped-flow
GCaMP6f
jGCaMP7f
jGCaMP8f
Normalized fluorescence
Time (ms)
D
Model fits (—) to jGCaMP8f ex vivo data
Paired protocol
1-2-10 protocol
80 ms
0.2 ΔF/F
100 ms
0.2 ΔF/F
E
Model States
Paired protocol
1-2-10 protocol
Fast fluorescent
80 ms
1 μM
100 ms
1 μM
Slow fluorescent
0.06 μM
0.09 μM
Slow, non-fluorescent
9 μM
8 μM
F
Excitatory cell-like simulation
200 ms
0.3 ΔF/F
BiophysSMC
LinearSMC
G
Inhibitory cell-like simulation
200 ms
0.3 ΔF/F
BiophysSMC
LinearSMC

Figure 4

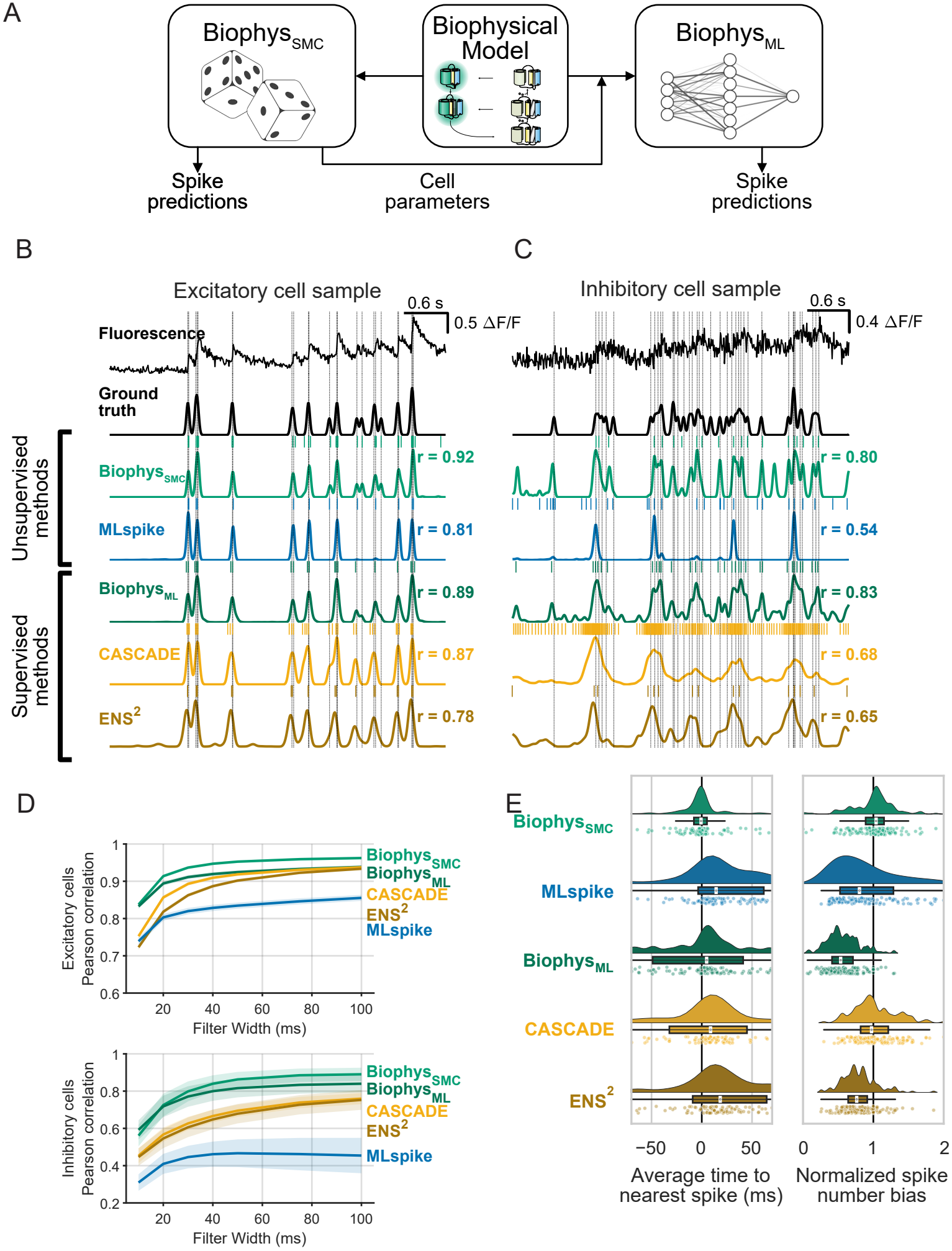
A
Biophys$_{SMC}$
Biophysical Model
Biophys$_{ML}$
Spike predictions
Cell parameters
Spike predictions
B
Excitatory cell sample
0.6 s
0.5 ΔF/F
Fluorescence
Ground truth
Unsupervised methods
Supervised methods
Biophys$_{SMC}$
r = 0.92
MLspike
r = 0.81
Biophys$_{ML}$
r = 0.89
CASCADE
r = 0.87
ENS^2
r = 0.78
C
Inhibitory cell sample
0.6 s
0.4 ΔF/F
r = 0.80
r = 0.54
r = 0.83
r = 0.68
r = 0.65
D
Excitatory cells Pearson correlation
Filter Width (ms)
Biophys$_{SMC}$
Biophys$_{ML}$
CASCADE
ENS^2
MLspike
Inhibitory cells Pearson correlation
Filter Width (ms)
E
Biophys$_{SMC}$
MLspike
Biophys$_{ML}$
CASCADE
ENS^2
−50 0 50
Average time to nearest spike (ms)
0 1 2
Normalized spike number bias

Supplementary Figure 1

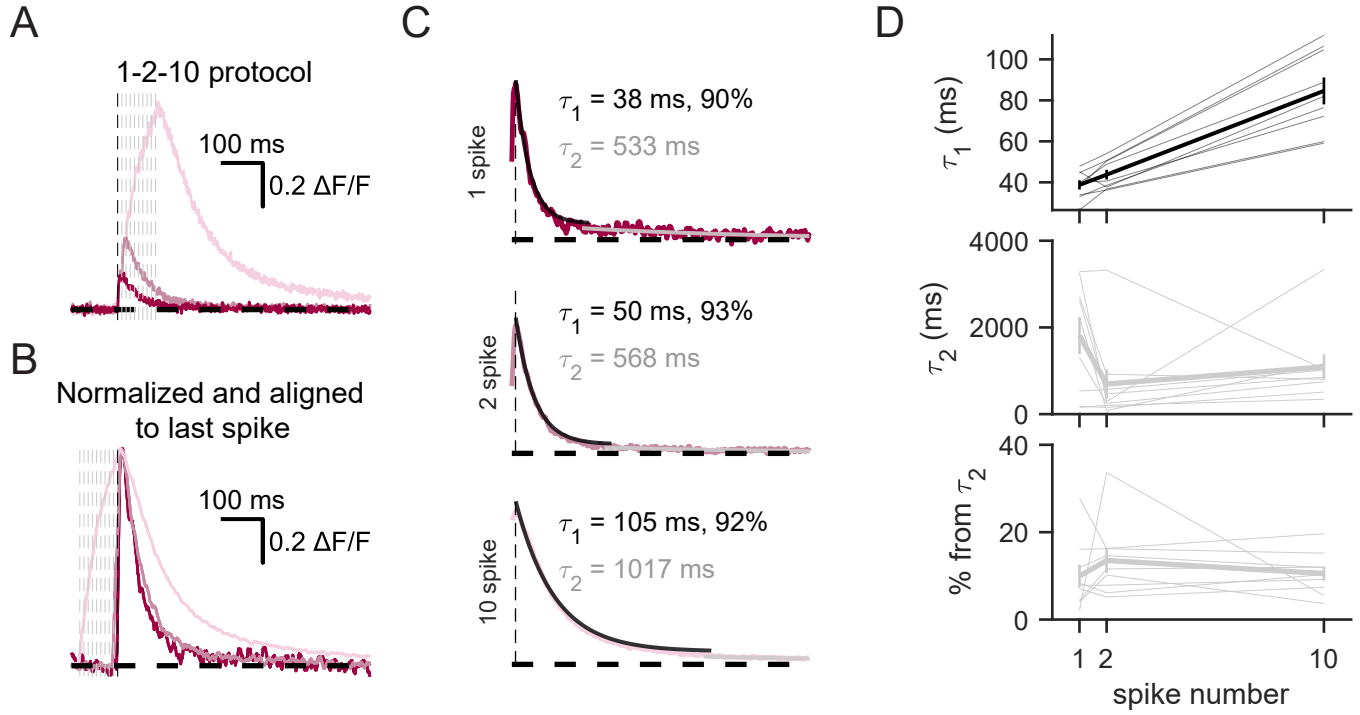

Supplementary Figure 2

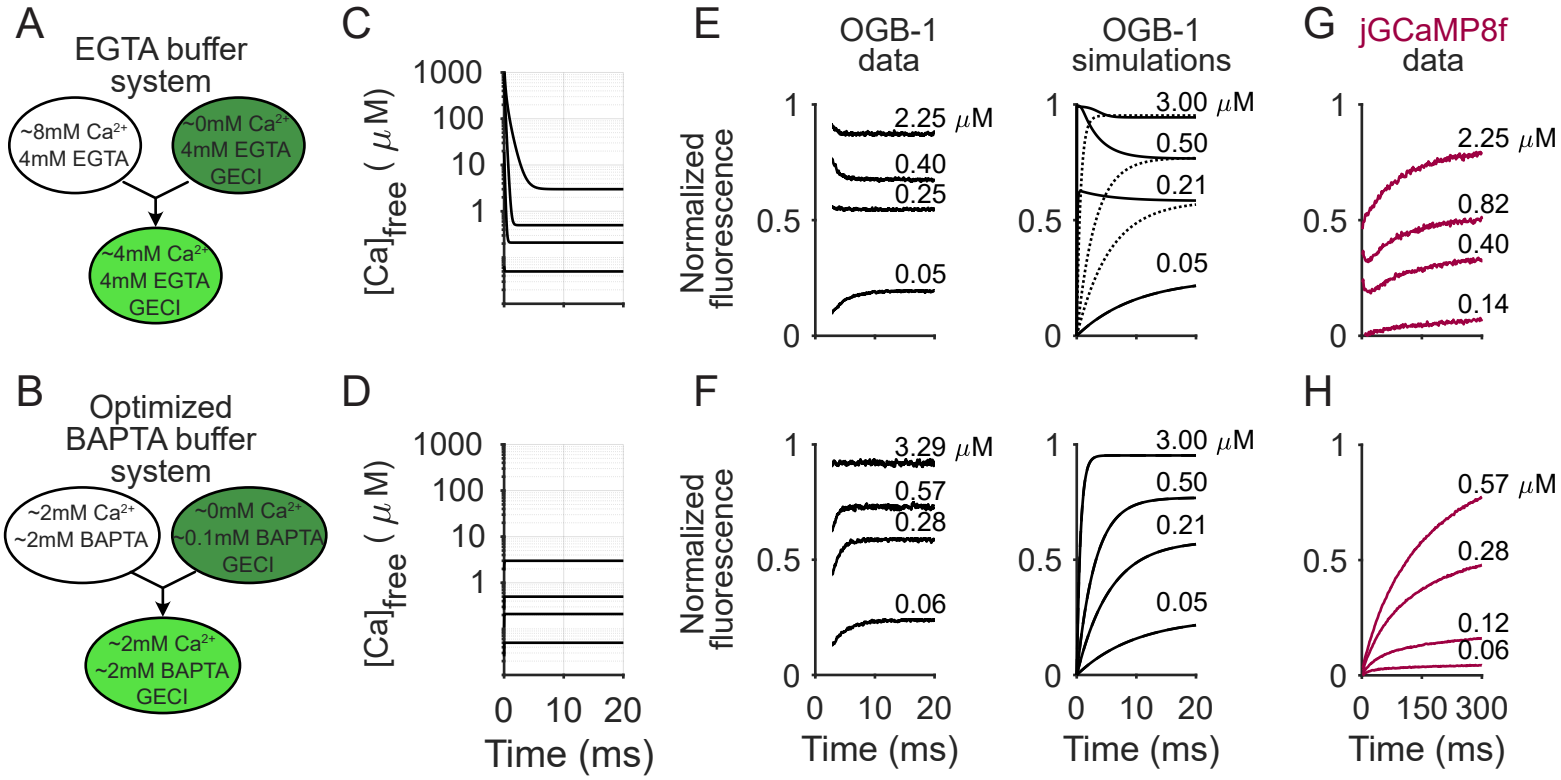

Supplementary Figure 3

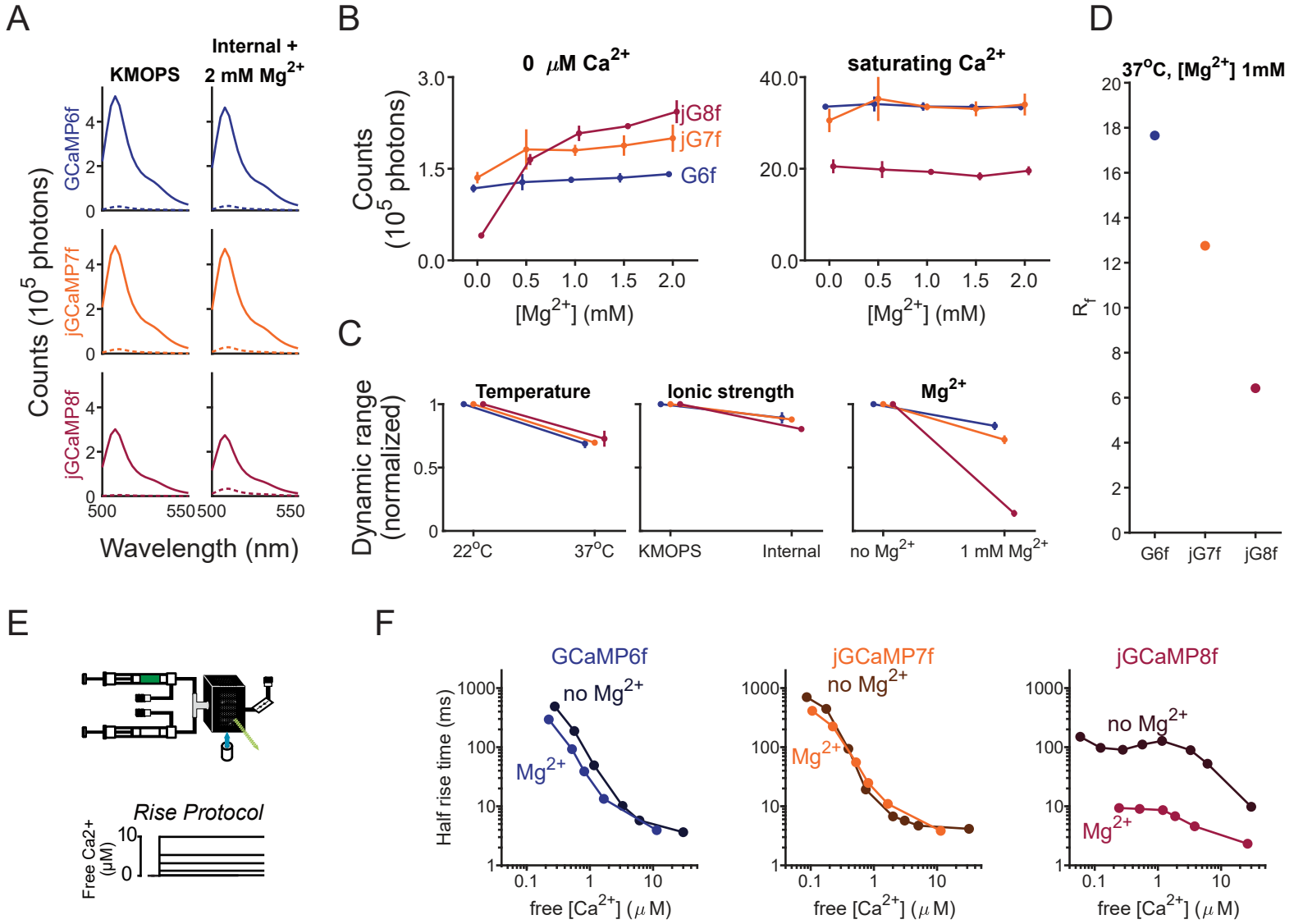

Supplementary Figure 4

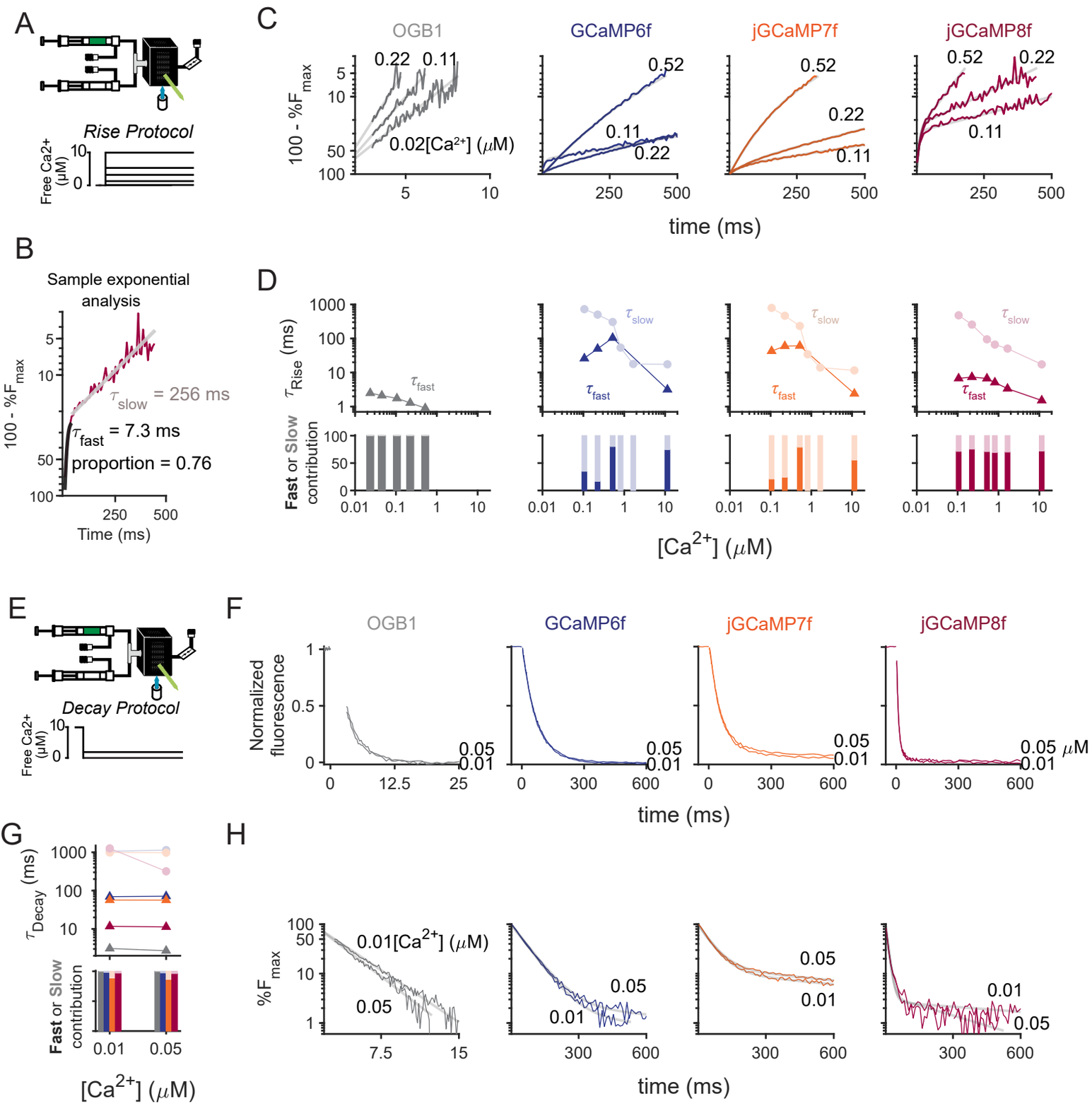

Supplementary Figure 5

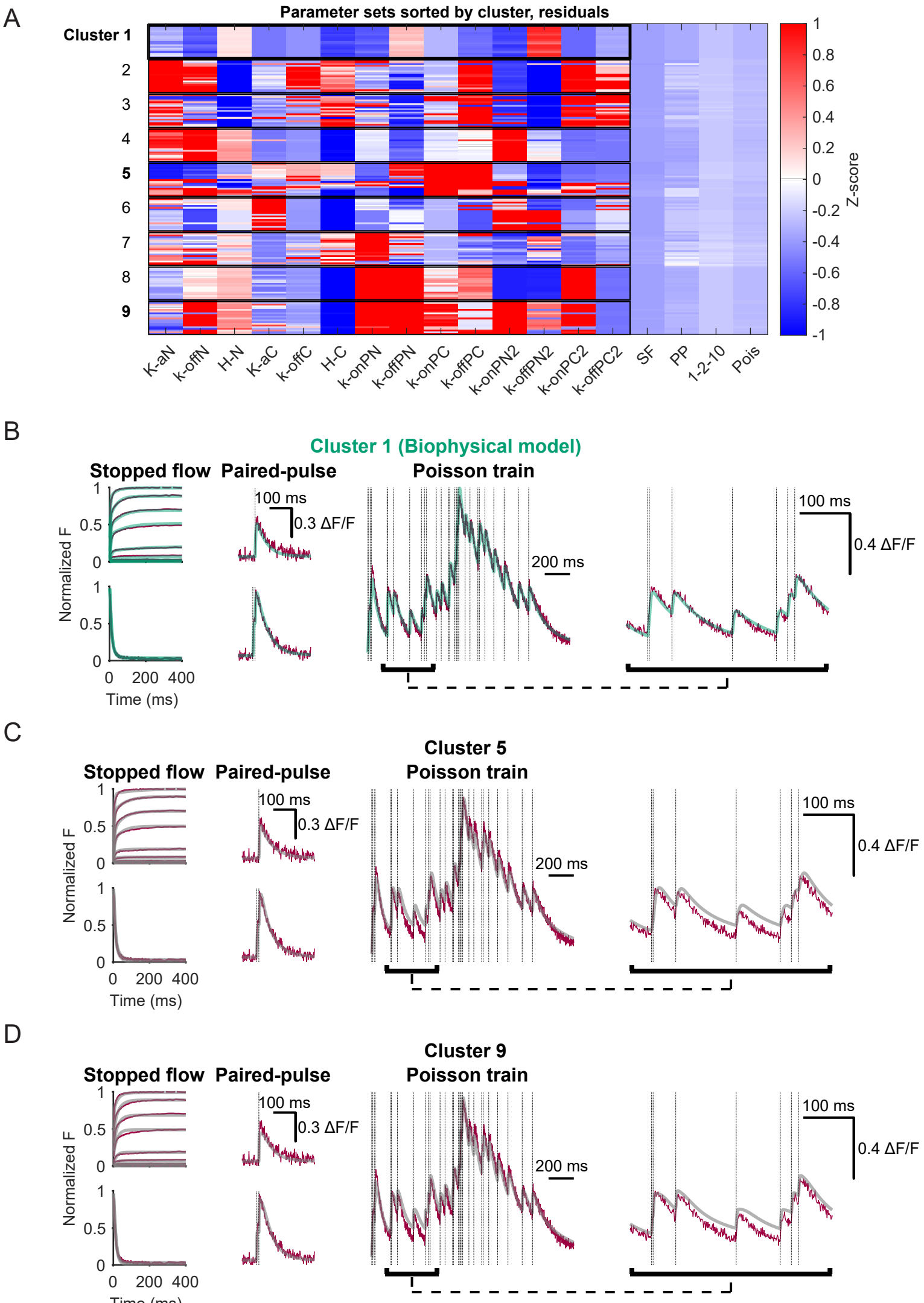

Supplementary Figure 6

A

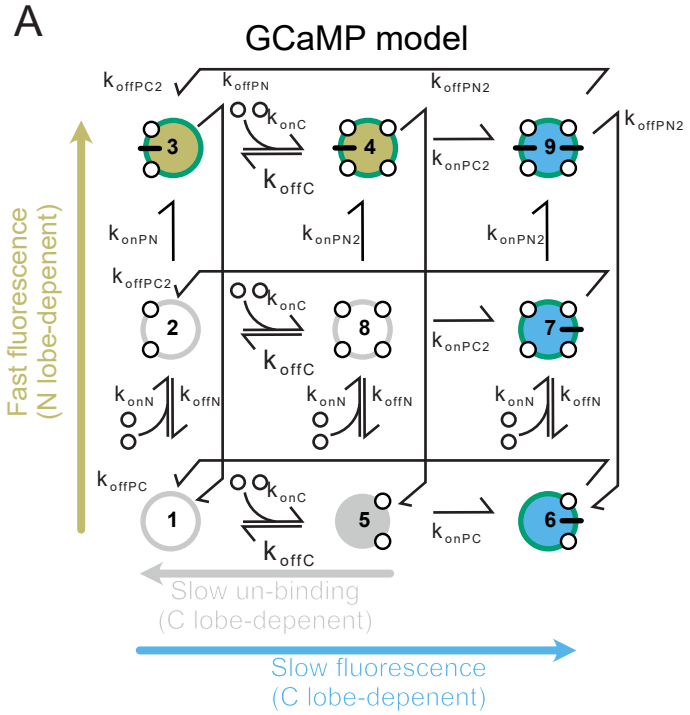

B

Parameter	Description	Units	GCaMP6f	jGCaMP7f	jGCaMP8f
K_{aN}	Affinity (N-terminal)	μM	0.87	1.69	0.51
k_{offN}	Off Rate (N-terminal)	s^{-1}	7.40	43.11	56.49
H_N	Hill Coefficient (N-terminal)	-	2.33	2.04	1.75
K_{aC}	Affinity (C-terminal)	μM	0.04	0.12	0.02
k_{offC}	Off Rate (C-terminal)	s^{-1}	7.13	18.12	0.46
H_C	Hill Coefficient (C-terminal)	-	2.61	2.80	0.96
k_{onPN}	On Rate (N-lobe bound)	s^{-1}	595.10	888.57	38.51
k_{offPN}	Off Rate (N-lobe bound)	s^{-1}	292.18	133.62	344.72
k_{onPC}	On Rate (C-lobe bound)	s^{-1}	2.79	0.26	0.14
k_{offPC}	Off Rate (C-lobe bound)	s^{-1}	795.81	4.51	36.79
k_{onPN2}	On Rate (Both lobes bound)	s^{-1}	10.04	30.79	59.63
k_{offPN2}	Off Rate (Both lobes bound)	s^{-1}	3.07	6.87	386.10
k_{onPC2}	On Rate (Both lobes bound)	s^{-1}	155.04	133.73	0.62
k_{offPC2}	Off Rate (Both lobes bound)	s^{-1}	11.37	22.58	29.38

C

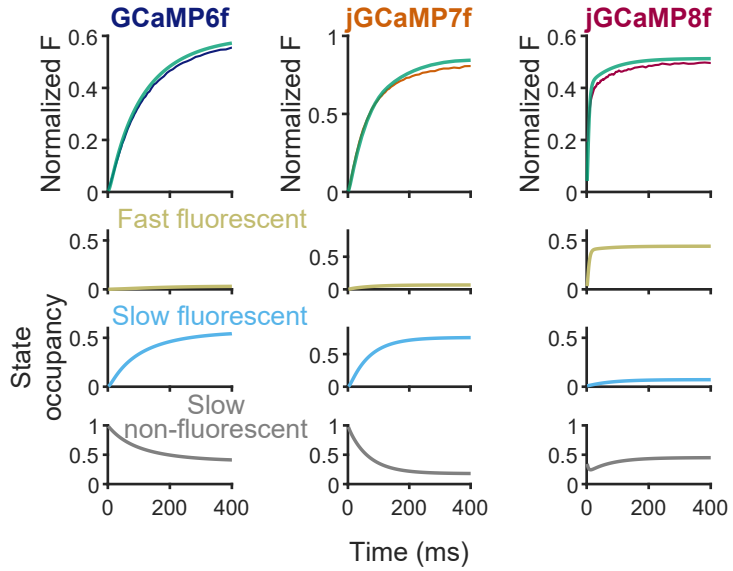

D

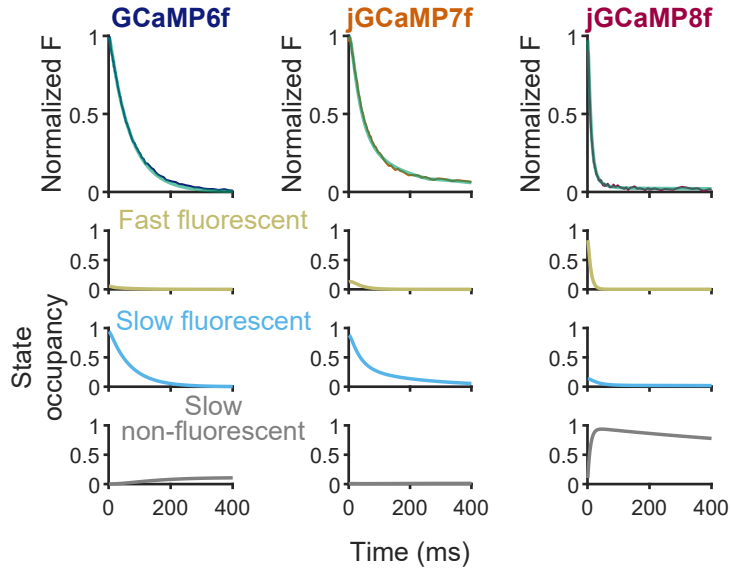

E

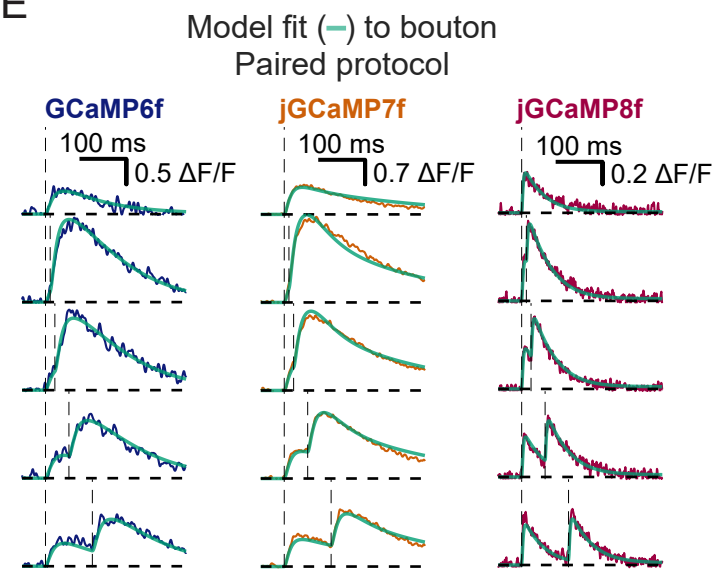

F

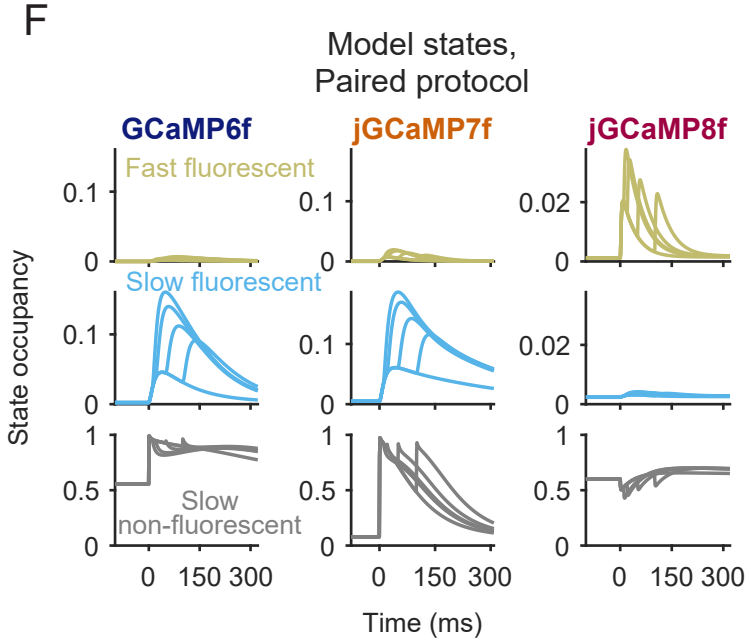

Supplementary Figure 7

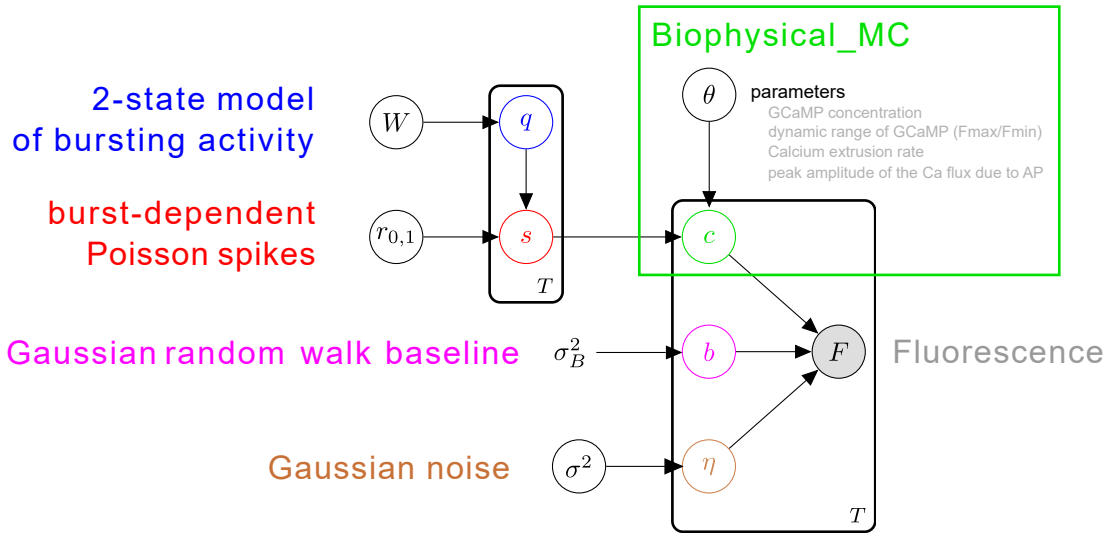
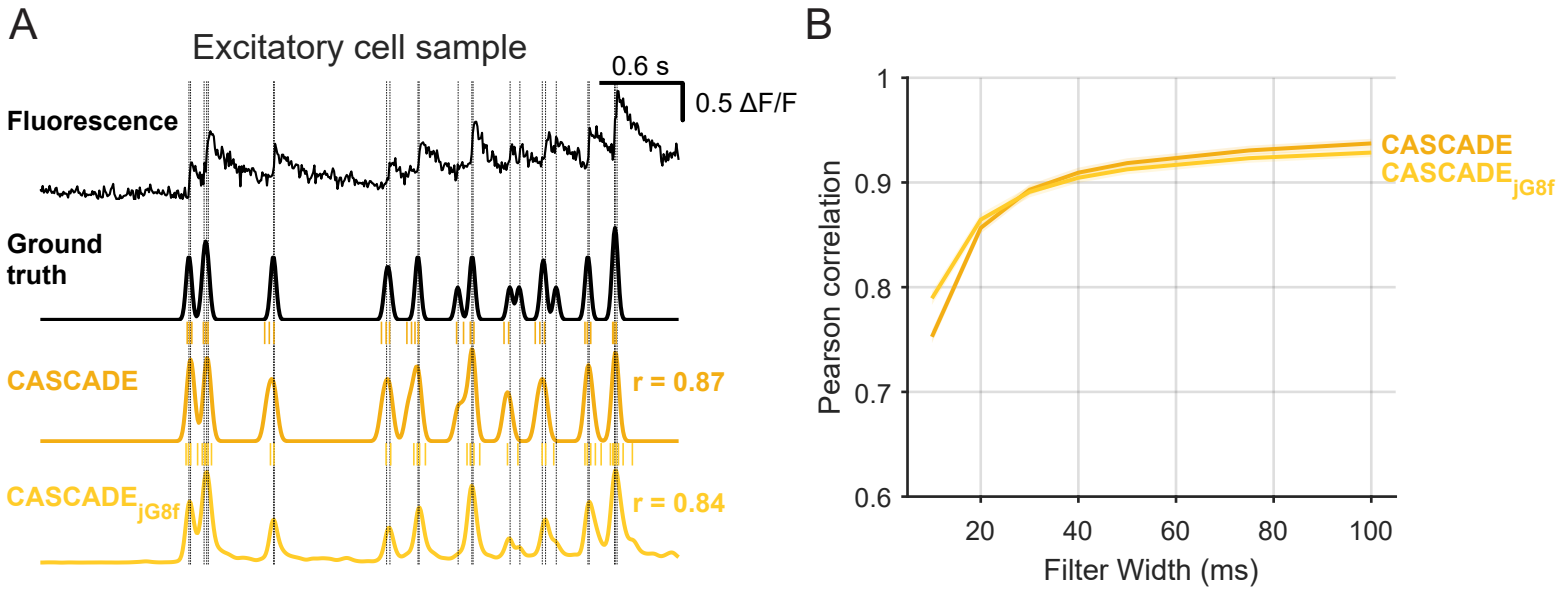
Supplementary Figure 8